Optimal Pulse Sequences for Magnetic Resonance Elastography

BY

TEMEL KAYA YASAR
B.S. (Middle East Technical University, Ankara, TURKEY) 2002
M.S. (Middle East Technical University, Ankara, TURKEY) 2006

THESIS

Submitted in partial fulfillment of the requirements
for the degree of Doctor of Philosophy in Mechanical Engineering
in the Graduate College of the
University of Illinois at Chicago, 2014

Chicago, Illinois

Defense Committee:
  Thomas J. Royston, Chair and Adviser, Bioengineering
  Ahmad A. Shabana
  Richard L. Magin, Bioengineering
  Laxman Saggere
  Dieter Klatt, Bioengineering

ProQuest LLC.
789 East Eisenhower Parkway
P.O. Box 1346
Ann Arbor, MI 48106 - 1346

To my son...

ACKNOWLEDGMENTS

Over the past six years I have received support and encouragement from a great number of individuals. Dr. Thomas J. Royston has been a mentor and a friend. His guidance has made this enjoyable and rewarding journey successful. His support and encouragement nourished my creativity and enthusiasm. I was fortunate enough to benefit from Dr. Richard Magins fathomless experience. I would be lucky if a *fraction* of his scientific talent and discipline were smeared on me. It was Dr. Dieter Klatts genius took us to take next level in Magnetic Resonance Elastography. I would like to express my deep gratitude to my dissertation committee: Dr. Ahmed A. Shabana, Dr. Laxman Saggere and Dr. Hansen Mansy. I am particularly grateful to Dr Robert Kleps for introducing me to the MRI Gods. I would like to thank to Eric Schmidt and David Mecha for realizing my the last minute eccentric machinery requests. I would like to offer my special thanks to my fellow graduate students those who have moved on and those who are still in the nest- Can Meral, Altaf Khan, Yifei Liu, Ziying Yin, Allen Ye, Zoujun Dai, Ying Peng, Steven Kearney, Spencer Brinker, The Great Benjamin I and Brian Henry for their invaluable help, support, feedback, and friendship. Finally, I wish to thank my wife, Demet, and my family for their prodigious support and encouragement throughout my study.

TKY

TABLE OF CONTENTS

TABLE OF CONTENTS (Continued)

LIST OF TABLES

TABLE **PAGE**

LIST OF FIGURES

LIST OF FIGURES (Continued)

LIST OF FIGURES (Continued)

LIST OF ABBREVIATIONS

MRI	Magnetic Resonance Imaging
TR	Repetation Time of pulse sequence
TE	Echo Time of pulse sequence
MRE	Magnetic Resonance Elastography
MEG	Motion Encoding Gradient
SDP	Selective Spectral Displacement Projection
SLIM	SampLe Interval Modulation
ULTIMATe	Unified sampLing Time Interval ModulATion
U-MRE	ULTIMATe MRE
PNR	Phase-to-Noise Ratio (Phase of complex MRI image)
SNR	Signal-to-Noise Ratio (Appendix A)

SUMMARY

Magnetic Resonance Elastography (MRE) is a non-invasive phase contrast MR imaging method that captures the three-dimensional harmonic wave propagation introduced into subject by external actuators. This wave propagation vector field is processed into stiffness maps of various kinds that are used to assess the pathological changes that cannot be detected otherwise with non-invasive imaging methods. As in all other MR imaging methods, long acquisition duration is one of the important limiting factors for MRE. There are different approaches to reduce the scan time, such as as reduced motion encoding MRE or fractional multi-frequency MRE; however, these methods are all at the cost of the reduced signal to noise ratio (SNR) or reduced phase to noise ratio (PNR). Recently we have introduced two accelerated MRE methods, which do not compromise SNR or PNR while reducing the acquisition time by a factor of three compared to the conventional MRE methods. The first one is Selective Spectral Displacement Projection (SDP) MRE method that can encode a mechanical motion of multiple frequency components at once. The second one is SampLe Interval Modulation (SLIM) MRE which can encode the mono-frequency motion in multiple directions concurrently. In this dissertation, I propose a final optimal method that integrates the technique developed in SLIM MRE into SDP MRE, namely Unified sampLing Time Interval ModulATion (ULTIMATe) MRE. This method is the optimal MRE method in the sense that it can reach the limit of time efficiency without sacrificing SNR and PNR. A new mathematical framework was introduced to accommodate all three methods while preventing any ambiguity which might otherwise can occur with the existing MRE notation.

CHAPTER 1

INTRODUCTION

Magnetic Resonance Elastography (MRE) is a phase contrast based MR imaging method that captures snapshots of harmonic wave propagation and encodes those wave images into the phase part of the complex MRI image (1). These phase contrast images are obtained by placing motion encoding gradients (MEG) synchronized with externally-driven harmonic wave motion into an MR imaging pulse sequence (Figure 5).

Changes in tissue structure and composition can alter its elastic and viscous properties (2). For centuries manual palpation has been used for detecting these changes successfully. However, manual palpation has limitations. First of all, organs behind bones or behind other organs cannot be palpated, such as brain, heart or lungs. In some cases fat tissue under the skin makes it very difficult for physicians to execute manual palpation successfully. Another issue is that changes in tissues should be sufficiently large enough for physicians to detect it. On top all those problems, manual palpation is subjective (3).

MRI is already known for its capability of detecting changes in tissue structure and composition (4). However, these changes may not be evident in conventional T1, T2 or diffusion-weighted MR imaging,etc (5) .

On the other hand, using MRE, as long as we can introduce mechanical motion into the target organ, can measure the viscoelastic properties of that organ remotely, or in other words without direct contact. Further, these measurements yield a quantitative viscoelastic map of the tissue based on the measured wave pattern such that numbers do not change from MRI system to MRI system because wave images are independent of relaxation parameters of the organ.

MRE is increasingly studied for detection, classification and monitoring of fibrotic diseases and injuries to almost all anatomical regions, including liver, brain, breast, muscle, kidney, heart, prostate and soft tissue (2) . MRE has also been utilized for non-invasive tracking the development of engineered tissues (6). Besides studies involving *in-vivo*, *ex-vivo* and *in-vitro* subjects, MRE is being used for increasing our understanding of relationship between mechanical parameters the MRE estimates and underlying mechanical structures (7; 8; 9).

An MRE scan at one frequency can only yield mechanical parameters for that particular frequency. These mechanical parameters are part of the projection of mechanical structure (or mechanical model) of the subject for a given frequency, as in eigenvalues of a system. In order to realize mechanical models, the mechanical parameters need to be determined at multiple frequencies. The number of those frequency points are determined by the unknown parameters in the mechanical model and the accuracy of the mechanical model increases as the frequency spans get wider. Therefore in order to collect mechanical parameters for a range frequencies and to understand the underlying mechanical structure of the subject, MRE scans need to be repeated at different multiple frequencies. Although, in some cases the repetition process can be eliminated at the cost of motion encoding efficiency, this will result in reduced SNR for the acquired wave image (10; 11). The SNR of the wave image eventually affects the error of mechanical parameter estimation, hence the error in mechanical model estimation.

Since its inception in 1995 (1), MRE has been constantly refined. Early in the development, scalar wave fields in two dimensions were acquired for a determination of the shear stiffness (a value closely related to magnitude of complex shear modulus) at one specific mechanical excitation frequency (1). Soon it was recognized that, since shear stiffness is a frequency-dependent quantity, additional information at multiple frequencies would be needed to establish tissue material parameters (e.g, by fitting rheological models to the measured, frequency-dependent wave quantities) (12; 13). In addition, (14) pointed out that, since a compressional wave is always present in an MRE experiment, it will introduce biases, when inverting the scalar wave images to determine tissue stiffness. To overcome this problem, the curl operator needs to be applied to the data, and this requires the acquisition of tissue vibrations along all three spatial directions inside a volume. A recent study demonstrated that the acquisition of all displacement components of a multifrequency vibration is very useful for increasing the spatial resolution and the quality of MRE-derived elastograms by applying a new least square error-based reconstruction method to 3D MRE data (15). Also, other current developments in both, multifrequency and monofrequency MRE propose the acquisition of three components of the displacement vector (16; 17; 18).

A single MRE image corresponds to a snapshot of the mechanical wave motion in tissue. A sequence of such snapshots is needed at different time steps to calculate the vibration harmonics of complex wave images. The array of images is then further processed to create elastograms. When performing MRE, depending on the specific approach, an acquisition block of four to eight individual phase-difference images is acquired in order to determine the complex wave image for one sensitization direction. For recording all components of the displacement vector, this acquisition block is typically repeated twice with MEGs applied along the remaining two coordinate axes resulting in a total of twelve to 24 phase-difference images.

Time is always the limiting factor on MRI technology. Generally speaking MRE is increasing the duration of an MRE scan compared with a standard MRI scan by a factor of 8 to 16. This longer scan duration causes problems on many different levels. First of all, longer scan times are not bearable nor feasible for most of the patients. Second, multiple scans over a longer time period means increased possibility of image mis-registration. Actually, in most of the cases image mis-registration already happens, so longer duration makes this misalignment even worse. This causes artifacts, decreasing SNR and introducing unknown errors in wave images. Third, cost per unit time of MRI scanner is already very high and this longer acquisition times reduces the chances of patient or hospital affording these scans or forces the hospital to speed up the scans by sacrificing the quality of scans.

In this dissertation, we present a novel MRE method and pulse sequence that can reduce the acquisition duration by a factor of three without sacrificing motion encoding efficiency. To be able to further compare this new method with the conventional methods, it is necessary to introduce a new term, the ”Motion Information”. A mechanical motion can be composed of multiple frequencies and/or multiple directions. A motion information is a wave image (single slice, multi slice or volumetric) obtained by encoding mechanical motion at only one the frequency across a particular direction. The MRE method we present in this study can acquire multiple motion information while keeping the total acquisition time compared the conventional

MRE. Although there are accelerated MRE methods presented in the literature, they are all at cost of motion encoding efficiency to save time. The method presented in this study, keeps the same motion encoding efficiency given the conditions such as, enough gradient power, enough mechanical actuation strength.

CHAPTER 2

PREVIOUS WORK

There are multiple approaches in the literature to speed up MRE. They can be categorized under two groups. In the first group (compromising accelerated methods), the methods reduce the scan time of MRE by compromising encoding efficiency, or the Phase-to-Noise Ratio(PNR) of the MRE images. In the second group methods (uncompromising accelerated methods), the methods keep the same encoding efficiency and PNR, but provide more information compared to the same duration of conventional MRE.

However, note that, the second group of methods are speeding up the total acquisition by generating more motion information in the same duration of conventional MRE, rather than reducing the acquisition time. In other words, the second group of methods are viable when one needs to encode more than one motion information (direction and/or frequency). For almost all of the cases, even in phantom studies, more than one motion information is needed. Therefore, it would be more beneficial to chose the second group methods over first group.

2.1 Compromising Accelerated Methods

2.1.1 RME Reduced Motion Encoding

The reduced motion encoding method was introduced in (10). This study focused on how to retrieve the motion information without aliasing or ambiguity with the minimum number of time steps. It considers both evenly distributed time steps and non-evenly distributed time steps. It also investigated the gradual increase in the wave image quality as new time steps are added to the overall scan. This allows the user to keep scanning until a desired quality of wave image is obtain and then stop there. Similar to wavelets, the user decides what is the acceptable quality and stops right at that point to avoid acquiring redundant information. But this method encodes one motion information at a time. Therefore, increasing the number of time steps would not allow user to encode more information, although a higher number of time steps would yield higher PNR.

2.1.2 Fractional Encoding

In conventional MRE the frequency of the motion encoding gradient (MEG) is matched to the frequency of the harmonic (monofrequency) vibration; therefore, the minimum echo time TE is increased by the duration of the MEG. This approach can suffer from low phase-to-noise ratio (PNR), particularly when low vibration frequencies are applied in tissues with relatively fast MR signal relaxation (short T2) such as occurs in the liver. Further, due to the long duration of the MEG, conventional MRE is not suitable for the examination of non-static structures such as the beating heart. To overcome this drawback, fractional encoding of harmonic motions, also referred to as fractional MRE, was introduced (11). This method utilizes MEGs with a duration shorter than the vibration period enabling fast data acquisition at the cost of a decreased motion encoding efficiency. Fractional encoding schemes were applied in order to examine the mechanical behavior of liver (12) and to reduce acquisition time in cardiac MRE (19).

Soon after, fractional MRE was refined for the simultaneous acquisition of multifrequency vibrations along one spatial dimension within one temporally-resolved MRE experiment (20). This approach is commonly referred to as multifrequency MRE. In multifrequency MRE, the frequency-independent material parameters of the tissue are calculated either by fitting the measured dispersion curves of the complex shear modulus to rheological models (20) or by solving the inverse problem of viscoelasticity reconstruction employing an algebraic least-square solution (21).

2.2 Uncompromising Accelerated Methods

2.2.1 SDP Selective Spectral Displacement Projection

In fractional encoding, studies employing the simultaneous acquisition of multifrequency vibrations have been performed solely in 2D; only displacements perpendicular to the image plane were measured. In spite of this limitation, the new insights gained by multifrequency 2D MRE are significant, as a correlation of brain mechanics with the aging brain (22) as well as with Multiple Sclerosis (23) and Normal Pressure Hydrocephalus (NPH) (24) has been revealed.

Recently, MRE studies were conducted in which the full 3D displacement field was acquired (17; 25; 14). 3D MRE exhibits several advantages when compared with 2D MRE. For example, in shear modulus-based approaches, the shear wave can be separated from the compression wave by applying the curl-operator to the displacement field (14). In addition, using 3D MRE, more realistic tissue models incorporating porosity can be considered (25) and tissue pressure changes can be identified by analyzing the divergence of the 3D displacement field (17).

However, the benefits of 3D MRE are offset by a longer measurement time which increases by a factor of three (the number of motion encoding directions) for each slice. Ultimately, for the derivation of frequency-independent material parameters beyond the shear modulus, multifrequency 3D MRE data sets will have to be acquired. This further prolongs the measurement time of conventional MRE, in which individual experiments are performed consecutively with various monofrequency vibrations. An alternative would be to simultaneously excite and encode multifrequency vibrations for each of the three motion encoding directions in successive steps, reducing the number of individual experiments to three temporally-resolved MRE experiments per image slice. However, this approach implies reduced motion sensitivity (motion encoding efficiency) at vibration frequencies that do not match the MEG frequency (11). Further, a higher number of MEG cycles does not increase the motion sensitivity, when the MEG and the spectral components of the vibration have different frequencies. This issue is less of a problem using low mechanical vibration frequency MRE ($f_m \leq 100$ Hz) as is typically performed in human scanners, where sufficient motion sensitivity can be provided using the fractional technique.

In high mechanical vibration frequency MRE, however, a larger number of MEG cycles needs to be applied for enhancing motion sensitivity, and the use of lower sensitivity fractional encoding schemes is not reasonable (26; 9). These limitations were motivation for SDP MRE in (27) to develop a fast algorithm for 3D motion encoding of a multifrequency signal composed of three superposed sinusoidal vibrations. SDP-MRE method reduces the measurement time without degrading motion sensitivity compared with conventional monofrequency MRE. In the

SDP-MRE approach, three MEGs are applied simultaneously in the Read, Phase and Slice directions. The sequence parameters are carefully chosen for exploiting the filter condition of MRE, which has previously been applied to observe higher harmonics of a nonlinear shear wave (28). This approach was named as selective spectral displacement projection (SDP)-MRE, since the filter condition is exploited for selecting one frequency in each spatial direction. The selected components are simultaneously encoded into the phase of the MR signal and the acquisition of temporally resolved phase images enables the decomposition of the individual components.

2.2.2 SLIM SampLe Interval Modulation

SampLe Interval Modulation (SLIM-MRE) introduces a new motion encoding concept for the displacement vector in monofrequency MRE (29). SLIM-MRE, is capable of acquiring all components of the displacement vector from only eight phase-difference images. In SLIM-MRE, the monofrequency vibration is encoded with different apparent frequencies for the three spatial directions by intentionally mismatching the sampling intervals with respect to the three spatial directions. In doing so, multidirectional data is encoded simultaneously and stored into the same k-space, which was considered to be unfeasible since the inception of MRE, 20 years. Due to the modulation of the sampling intervals, the individual displacement components can be decomposed by applying a Fourier transform.

CHAPTER 3

BACKGROUND

3.1 Wave Propagation in Viscoelastic Materials

For an isotropic, homogeneous, viscoelastic compressible medium one can use the following formulation of the equation of motion for small perturbations about an operating point (30).

$$(\lambda + \mu)\nabla\nabla \cdot \mathbf{u} + \mu\nabla^2 = \rho\frac{\delta^2\mathbf{u}}{\delta t^2} \tag{3.1}$$

Here, u is the displacement vector, ρ is the density of the medium, $\frac{\partial}{\partial t}$ denotes a derivative with respect to time, ∇^2 is the spatial Laplacian operator dependent upon the chosen coordinate system, and λ and μ are the Lamé constants of the medium for a given frequency. In general Lamé constants are actually complex functions of frequency where real part signifies storage and imaginary part denotes loss. Parameter μ is also called shear modulus and this will be the name commonly used in the MRE literature. For a linear viscoelastic integer Voigt material model, the rate-dependent Lamé constants are expressible as $\lambda(t) = \lambda_0 + \lambda_1\frac{\partial}{\partial t}$ and $\mu(t) = \mu_0 + \mu_1\frac{\partial}{\partial t}$ where $\lambda_0, \lambda_1, \mu_0$ and μ_1 are coefficients of volume compressibility, volume viscosity, shear elasticity and shear viscosity, respectively.

The wave equation in (Equation 3.1) is widely used in stiffness map estimations of various kinds. Wave images obtained from the MRE scans provides $\mathbf{u}$ information. Since $\mathbf{u}$ is a harmonic motion of known frequency and assuming we know the density ρ, we can solve (Equation 3.1) for remaining constants. Depending on the completeness of harvested motion information, such as one dimensional or three dimensional, multiple or single slice of $\mathbf{u}$, several simplifications needed to be done in order solve (Equation 3.1). In some cases, due to strong simplifications Lamé parameters are omitted or ignored out of wave equation and stiffness maps are estimated only for the shear modulus.

3.2 Mechanical Models

With regard to μ, it was observed in this study and in many other materials in other studies that the simple two-element Voigt or Maxwell models for shear viscoelasticity do not accurately capture material shear dynamic behavior, in terms of experimentally-measured responses to various elementary excitation waveforms, such as step inputs or periodic or random inputs with broad spectral content (31; 32). Complex arrangements of multiple elastic (springs) and viscous (dashpot) components may be employed empirically in order to more closely match experimentally measured complex-valued shear modulus values over a range of frequencies. For example, the Standard Linear Solid (SLS) Model, also known as the Kelvin or Zener model, consists of a parallel combination of a Maxwell element (spring and dashpot in series) with a spring. The three-element SLS model has more flexibility in representing dynamic viscoelasticity over a broad frequency range as compared to the Voigt model. A more complex example is the Generalized Maxwell model, comprised of a parallel combination of an SLS and a single or multiple Maxwell models. Although it is known that Maxwell and Voigt models can not represent wide frequency range viscoelastic responses, they have been included in the analysis for the sake of completeness. Even if adding more components to the model increases the ability of the model to mimic experimental measurements, this improved ability is at the expense of added model complexity and potentially non-uniqueness. Instead of increasing the constitutive model complexity by increasing the number of components that comprise it, an alternative is to consider that the material may exhibit rate-dependent shear deformation that is best described by a single element, comprised of two constants, μ_α and α (20), whose behavior lies somewhere between Hookean solid and Newtonian fluid. Specifically, fractional order viscoelasticity (a springpot) can be specified as shown in the second term of the following:

$$\mu = \mu_0 + \mu_\alpha \frac{\partial^\alpha}{\partial t^\alpha} \quad , 0 < \alpha < 1 \tag{3.2}$$

(Equation 3.2) is referred to as a fractional order Voigt model. The mathematics above extends the Rouse model (33) of polymer relaxation to a continuous distribution of relaxation times, which falls off at higher frequencies as a fractional order power law. It is commonly used to describe the elastic properties of rubbery and glassy polymers (34), such as Ecoflex, a type of polysiloxane. It can be shown that this type of relation results asymptotically when using a ladder-like fractal arrangement of integer-order elastic and viscous components (35). Indeed, such an arrangement might be rationalized on the grounds that it represents multiscale rate-dependent stress-strain interactions that one would inherently expect in some materials with complex multiscale cellular and extracellular structure, such as biological tissues. Furthermore, suitably defined fractional derivatives do not pose significant difficulty mathematically for wellconditioned functions. In this study the Weyl definition of the fractional order derivative is used, which for harmonic functions such as $f(t) = e^{j\omega t}$ has the property that

$$\frac{\partial^\alpha e^{j\omega t}}{\partial t^\alpha} = (j\omega)^\alpha e^{j\omega t} \tag{3.3}$$

The expression in (Equation 3.3) is still linear in nature and thus all rules and techniques afforded such relations, such as the validity of superposition, reciprocity, the Laplace and Fourier transforms, with associated transfer and frequency response functions, are all still valid (36). In the Laplace (s) and frequency ($j\omega$) domains where $j = \sqrt{-1}$ and ω is the circular frequency, (Equation 3.2) respectively becomes

$$\mu = \mu_0 + \mu_\alpha (s)^\alpha \tag{3.4a}$$

$$\mu = \mu_0 + \mu_\alpha (j\omega)^\alpha \tag{3.4b}$$

Note a significant attribute of such fractional representations is that the temporal response takes on characteristics of power-law behavior as opposed to the exponential response that one obtains with the conventional Voigt representation. A power-law response in fact has been observed in a number of biological and non-biological materials, further motivating this type of model (32; 37).

Also note that, in the frequency domain, we have $\mu(\omega) = \mu_\mathrm{R}(\omega) + j\mu_\mathrm{I}(\omega)$ (storage and loss shear moduli) and both μ_R and μ_I are independent of what type of viscoelastic model is used and whether it is of integer or fractional order.

3.3 Conventional MRE

Magnetic Resonance Elastography is an MR imaging method that creates a stiffness map of the target subject. Stiffness map can be composed of various values depending on which parameter is estimated and this parameter is decided according to imaging the needs and available data. MRE is composed of two stages: imaging of wave propagation and reconstruction of the stiffness map. The wave imaging method is based on a phase contrast MRI method that enables taking snapshots of the displacement vector field during steady state harmonic mechanical motion. Reconstruction of the stiffness map can be done with several different inversion algorithms depending on the motion information encoded into the MR image (38). The stiffness map yields one or more mechanical properties, such as shear modulus, shear stiffness, Lamé parameters, etc., of the material under investigation.

3.3.1 Encoding Motion Information into the MR Image

Motion information is encoded into the phase part of a complex MRI image. In order to achieve this, harmonic gradient pulse shapes are inserted into a conventional MR imaging pulse sequence. These gradient pulse shapes are called Motion Encoding Gradients (MEG) (Figure 5).

Motion accumulates as an additional phase, ϕ, into the complex MRI image. This extra phase accumulation is equal to the time integral of the projection of displacement onto the MEG direction multiplied by gyromagnetic ratio. The duration of integration T is usually an integer multiple, M, of period, 1/f, of the mechanical motion.

$$\phi = \gamma \int_0^T \mathbf{g}(t) \cdot \mathbf{u}(t) dt, \ \ T = \frac{M}{f}, \ \ M \in \mathbb{Z}^+ \tag{3.5}$$

There are two outcomes of (Equation 3.5). First , a one-dimensional projection of a three-dimensional harmonic displacement can be encoded into the phase image by placing MEGs in that particular dimension. So if three-dimensional displacement vector field is needed, all three dimensions should be encoded independently. Second, the frequency of both motion and MEG should be the same in order to achieve maximum motion encoding efficiency because the MEG and displacement vectors are being integrated over time. An example of phase accumulation for one-dimensional case is given in Figure 1. Numbers and scales are not important for this example but it should be noted that as the integration time increases, the total accumulated phase increases. On the other hand if there is a frequency mismatch between mechanical motion and MEG, phase accumulation will not be monotonically increasing with time, as can be seen from Figure 2. In Figure 2, the time axis was chosen to be longer than in Figure 1 in order to demonstrate phase accumulation is bounded to an upper limit.

The importance of mismatched frequency is, for some clinical cases, due to excessive increase in echo time for the given operating frequency, the frequency of the MEG cannot be matched to the frequency of mechanical motion. This type of motion encoding is called fractional encoding (11). As can be seen from Figure 2 one of the main drawbacks of this method is that it is not possible to increase phase accumulation with longer MEG durations.

Almost all of the time, there will be extra random phase accumulation originating from various factors including but not limited to inhomogeneous material, gradients and RF fields. In order to eliminate this random phase accumulation, the same scan needs to be repeated while reversing the sign of MEGs. Since MEGs are harmonic functions, this sign inversion is

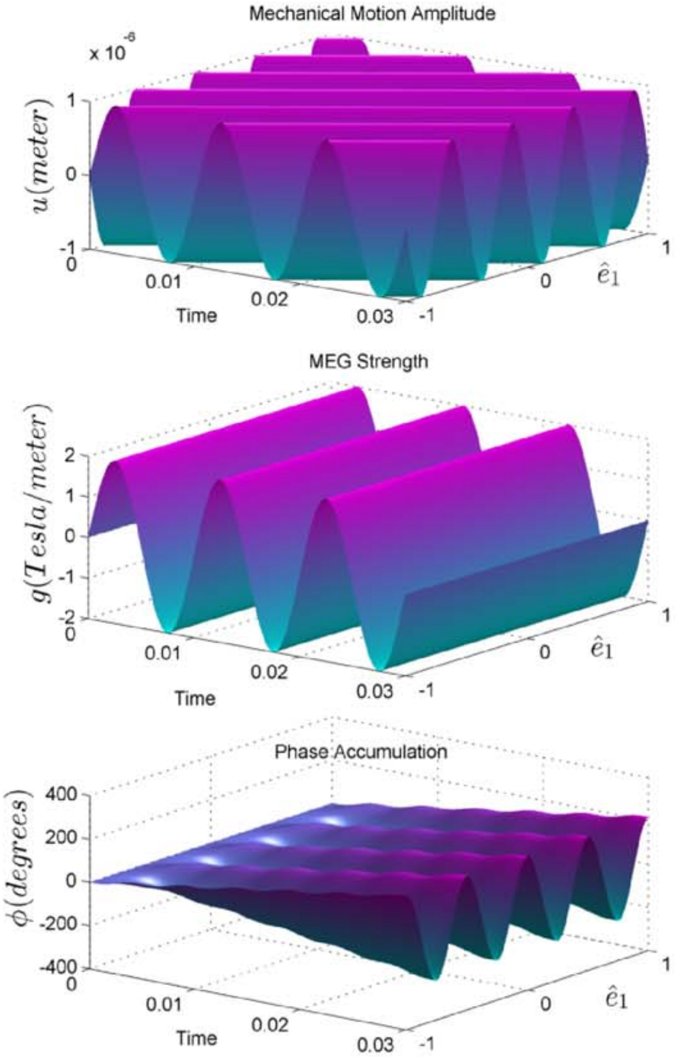

Figure 1: Top figure shows one-dimensional mechanical shear wave propagation. The wave is propagating in the $\hat{e}_1$ direction with a frequency of 100 Hz but particle motion is in the direction $\hat{e}_2$, where $\hat{e}_1 \perp \hat{e}_2$ ($\mathbf{u}(t) = 10^{-6}\sin(2\pi(100t - ke_1))\hat{\mathbf{e}}_2$). Middle figure shows the MEG of same frequency cycling in time along $\hat{e}_2$ axis ($\mathbf{g}(t) = 2 \times \sin(2\pi f t)\hat{\mathbf{e}}_2$). Bottom figure show phase accumulation over time as given in (Equation 3.5).

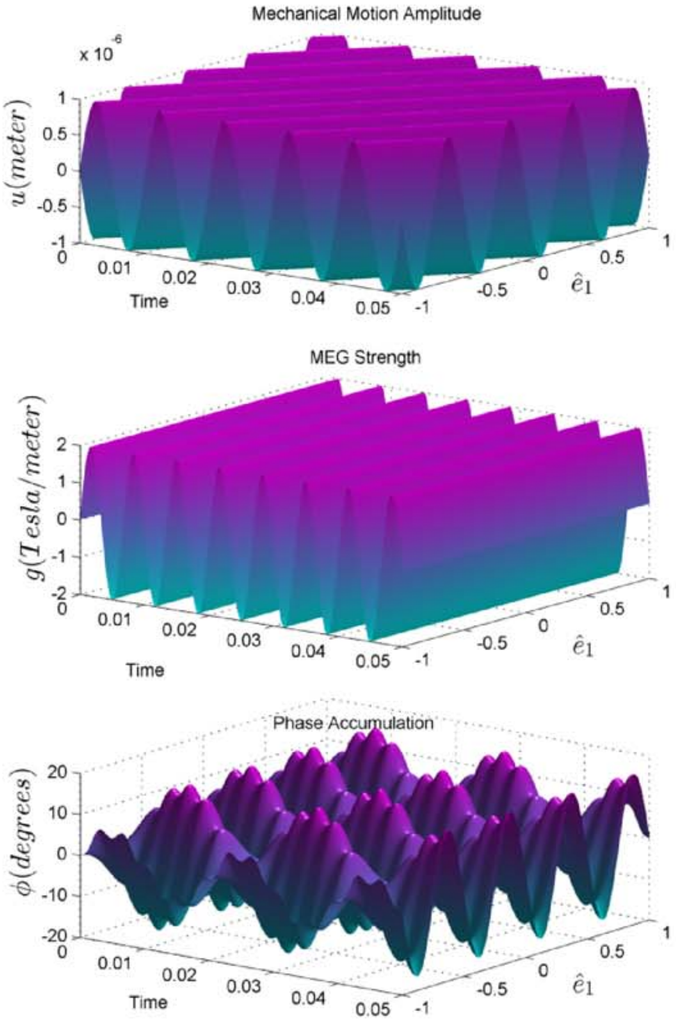

Figure 2: Top figure shows one-dimensional mechanical shear wave propagation. The wave is propagating in the $\hat{e}_1$ direction with a frequency of 100 Hz and particle motion is in the direction $\hat{e}_2$, where $\hat{e}_1 \perp \hat{e}_2$ ($\mathbf{u}(t) = 10^{-6}\sin(2\pi(100t - ke_1))\hat{\mathbf{e}}_2$). Wave is propagating in $\hat{e}_1$ direction but it moves in an orthogonal direction $\hat{e}_2$, $\hat{e}_1 \perp \hat{e}_2$. Middle figure shows the MEG of different frequency cycling in time along $\hat{e}_2$ axis ($\mathbf{g}(t) = 2 \times \sin(2\pi 150t)\hat{\mathbf{e}}_2$). Bottom figure show phase accumulation over time.

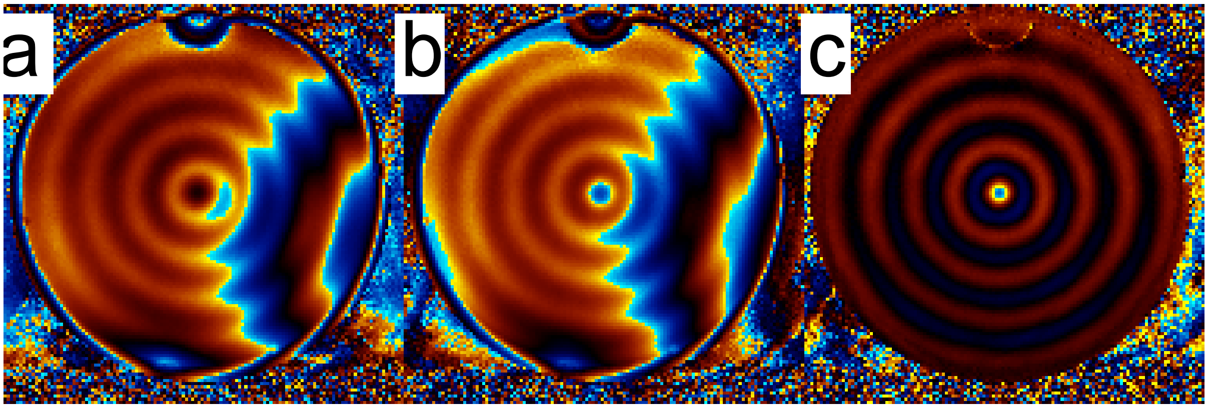

Figure 3: (a). Phase image of an MRE scan (b). Phase image of an MRE scan, where MEGs are shifted 180°. (c). Difference between part a and part b, where all common phase accumulations cancelled each other out but phase accumulation due to harmonic motion was added up. This image is called Wave Image of one time step.

mathematically equal to 180° phase shifting of original MEG, therefore we call the first scan as 0° phase image (Figure 3a) and the second scan as 180° phase image (Figure 3b). When the algebraic difference of these images are taken, the resultant image will be a linear function of displacement function (Figure 3c).

Although one wave image is enough to capture an instant of mechanical wave motion, it is not enough to separate more than one wave passing through the same voxel. To demonstrate this problem, one-dimensional wave propagation domain will be used in the following derivations. Extending these derivations into the two-dimensional case will be clear at the end of the derivation. Assuming that there are two waves propagating in opposite directions with different amplitudes and phase. With one snapshot of wave motion it is not possible to separate them from each other. However, if we know how this wave image changes in time, it would be possible recover individual waves. Mathematically speaking if the summation on two waves are denoted by function $y(k)$

$$
\begin{aligned}
y(k) &= A_1\cos(kx) + A_2\cos(-kx+\theta) &\text{(3.6a)}\\
&= A_1\cos(kx) + A_2\cos(+kx-\theta) &\text{(3.6b)}
\end{aligned}
$$

where k is the wave number and θ is the random phase value. For a single snapshot there is no time information and it is not possible to recover A_1 and A_2. But, if we have time dependency in the function y as

$$
\begin{aligned}
y(t,k) &= A_1\cos(\omega t + kx) + A_2\cos(\omega t - kx + \theta) &\text{(3.7a)}\\
&= A_1\frac{e^{j(\omega t+kx)} + e^{-j(\omega t+kx)}}{2} \\
&\quad + A_2\frac{e^{j(\omega t-kx+\theta)} + e^{-j(\omega t-kx+\theta)}}{2} &\text{(3.7b)}\\
&= \frac{e^{j\omega t}}{2}\left[A_1e^{j(kx)} + A_2e^{j(-kx+\theta)}\right] \\
&\quad + \frac{e^{-j\omega t}}{2}\left[A_1e^{j(-kx)} + A_2e^{j(kx-\theta)}\right] &\text{(3.7c)}
\end{aligned}
$$

it would be possible to calculate A_1, A_2 and θ via analytical signal of $y(t,k)$ which is denoted by $y_+(t,k)$. In general analytical signals can be written as a summation of the signal itself (y) plus the Hilbert transform of signal ($\hat{y}$) multiplied by j,where $j =\sqrt{-1}$ Equation 3.8 (39).

$$y_+(t,k) = y(t,k) + j\hat{y}(t,k) \tag{3.8a}$$

$$\begin{aligned} &= [A_1\cos(\omega t + kx) + A_2\cos(\omega t - kx + \theta)] \\ &\quad j[A_1\sin(\omega t + kx) + A_2\sin(\omega t - kx + \theta)] \end{aligned} \tag{3.8b}$$

$$\begin{aligned} &= [A_1\cos(\omega t + kx) + jA_1\sin(\omega t + kx)] \\ &\quad [A_2\cos(\omega t - kx + \theta) + jA_2\sin(\omega t - kx + \theta)] \end{aligned} \tag{3.8c}$$

$$= A_1 e^{j(\omega t + kx)} + A_2 e^{j(\omega t - kx + \theta)} \tag{3.8d}$$

$$= e^{j\omega t}\left(A_1 e^{-jkx} + A_2 e^{-j\theta} e^{jkx}\right) \tag{3.8e}$$

Compared to the Fourier transform of (Equation 3.7c), (Equation 3.8e) is half of the spectrum. The term $A_1e^{-jkx} + A_2e^{-j\theta}e^{jkx}$ in (Equation 3.8e) can be obtained if Fourier transform of the signal $y(t,k)$ is obtained and negative frequencies are omitted. Another Fourier transform has to be taken in the spatial domain (along x in one dimensional case) in order to separate A_1 from A_2 and to calculate θ. To summarize the process for the two-dimensional case in four steps:

1. Take 1-D Fourier transform across time domain
2. Take positive frequency part of transformed signal and omit negative frequency part

3. Take 2-D Fourier transform across spatial domain
4. Select particular region in spatial frequency domain to separate different directions from each other

Since it is impossible to obtain $y(t,k)$ in a continuous interval, we have to sample it for a finite number of time points over a finite duration. In the MRE literature the number of time points is called Number of Time Steps (NoTS). In Figure 4(a-h), a wave image can be seen at 8 equal distant time steps. Combination of the same pixel across all slices is shown in Figure 4(i-p) with a red line piercing through wave images across the time domain. The amplitude of those point are plotted as red circles in Figure 4(q). Even if one takes a discrete Fourier Transform instead of continuous one, it is still possible to obtain the complex term, $A_1 e^{-jkx} + A_2 e^{-j\theta} e^{jkx}$. Once this term is obtained the discrete Fourier transform will be taken in discrete spatial domain since wave images have finite resolution. Then, if we want to find A_1 we take negative spatial frequencies, otherwise we take positive spatial frequencies for A_2 and θ.

The difference between wave image and analytical wave image is very important in SDP, SLIM and U-MRE as well as in conventional MRE. Wave images are obtained by subtraction of 0° and 180° phase images from each other (Figure 3); they are real valued and there would be NoTS many wave images. On the other hand, the analytical wave image is the complex coefficients of one of the frequency bins in the frequency domain. Since frequency domains are complex conjugate around π for real values functions, the number of unique analytical wave images that can be obtained would be half of NoTS (or half of NoTS-1 if it is an odd integer). Although it looks like there is information loss due to the statement above, there is not. Wave

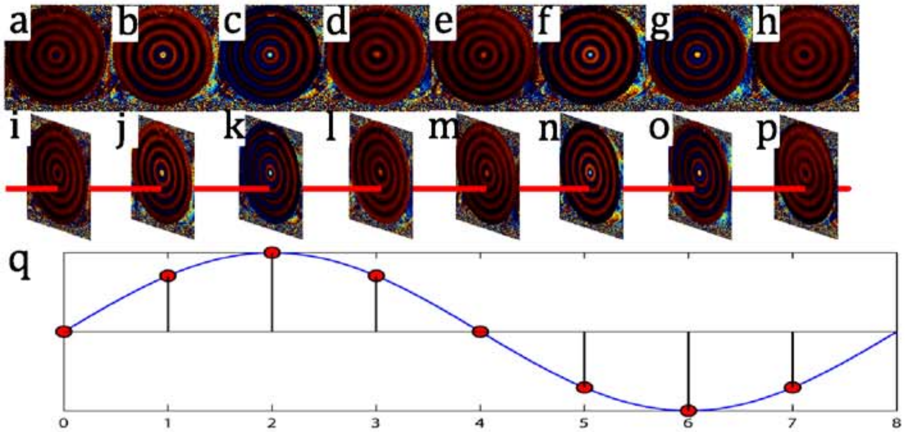

Figure 4: [a-h] Wave images of mechanical wave propagation at 8 equally separated time steps over a period. [i-p] Same pixel is chosen in space for all wave images. [q] Amplitude of the pixel chosen is indicate by red circles and it can be seen that these pixels are uniform samples of a harmonic wave form over a period.

images are all real valued images. They have no imaginary part. On the other hand, analytical wave images are all complex valued, so each pixel on each frequency bin has two elements, the real and the imaginary parts. Therefore even if we omit the negative frequency part, we do not lose any information. Note that, usually only the real part of analytical wave image is displayed in the literature and so in this dissertation. But it must be kept in mind that it is always a complex image.

When it comes to creating a wave image at different time steps, a time difference or a phase difference (assuming steady state harmonic motion is reached) is put between mechanical motion and MEG. In Figure 5 phase difference between MEG(s) and mechanical motion is set

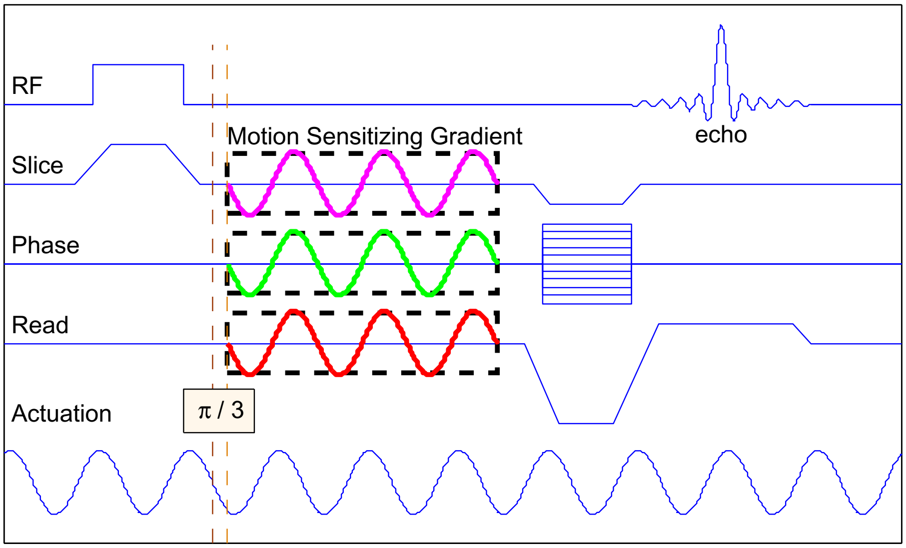

Figure 5: Phase difference between MEG(s) and mechanical motion. One or more MEG(s) can be active depending on the direction of motion to be encoded.

to $\pi/3$ radians. Depending on the constraints, either or both of mechanical motion and MEG can be shifted. For the sake of simpler mathematical notation, the angular phase of the MEG function is set to 0 or π radians when it starts. This is also useful for practical execution for avoiding discontinuities on the gradient shape. Although in 1^{st} order gradient nulling techniques (40) the angular phase starts at $\pi/2$ radians, we won't introduce any moment nulling technique in this study. However, the ideas introduced in this dissertation are still valid for gradient shapes for moment nulling.

Although we can shift either or both MEG and mechanical wave, for the sake of simplicity, the phase of mechanical motion was kept constant throughout the derivations. This simplification doesn't effect the validity of the methods described in this study. In practice phase of the mechanical motion can also be shifted with respect to phase accumulation.

The phase accumulation formula for a general case is given below. Here the delay introduced to MEG(s) is denoted by s.

$$\phi(s) = \gamma \int_{s}^{s+T} \mathbf{g}(t-s) \cdot \mathbf{u}(t) dt \quad , \qquad \begin{aligned} s &= \frac{n}{f_m N} \quad , n \in \mathbb{Z}^+ \\ \mathbf{u}(t) &= u_0 \sin(2\pi f_m t + \theta_u) \hat{\mathbf{e}}_{\mathbf{m}} \\ \mathbf{g}(t) &= G_0 \sin(2\pi f_g t + \theta_g) \hat{\mathbf{e}}_{\mathbf{g}} \end{aligned} \tag{3.9}$$

$$\phi(s) = \phi_0 \cos(2\pi f s + \theta) \quad \text{,when } \ f_m = f_g = f \tag{3.10}$$

,where θ is the phase accumulation, $\mathbf{g}$ is the vectoral gradient shape function, $\mathbf{u}$ is the displacement vector, s is the starting time of MEG(s), T is the duration of MEG(s), f_m is the frequency of mechanical motion, f_g is the frequency of the gradient shape, θ_u phase of mechanical motion, θ_g phase of gradient shape, $\hat{\mathbf{e}}_{\mathbf{m}}$ and $\hat{\mathbf{e}}_{\mathbf{g}}$ are unit direction vectors of mechanical motion and gradient shape respectively, and t is the time domain variable.

Given that the mechanical motion frequency and gradient shape function frequency are equal, the resultant accumulated phase is also going to be a harmonic function at the same frequency with a certain phase θ. This phase of the phase accumulation function is a function of position for a particular voxel and phase difference between mechanical motion and gradient shape. The amplitude of this phase accumulation, ϕ_0, is a function of displacement amplitude, gradient strength, duration, gyromagnetic ratio and angle between displacement vector and gradient shape vector (Equation 3.10).

After $\phi(s)$ is obtained the same scan is repeated with inverted gradient shapes. The first one is called 0° wave image and the later one is called 180° wave image. As described earlier (Figure 3), these two phase images are subtracted from each other to obtain the wave image of a time step that belongs to the time delay of s.

3.3.2 Stiffness Map Estimation

A stiffness map can be estimated by processing the displacement vector field obtained with MRE pulse sequence given some mechanical properties of the target object, such as its Poissons ratio, density, and making assumptions about steady state harmonic motion, porosity (or no porosity) and local homogeneity. Although stiffness maps were used in order to compare the performance of the new algorithm with conventional ones, the details of the methods are out of scope of this dissertation. However, the major stiffness map estimators are listed below in order to give basic insight to the reader. There are mainly three types of stiffness estimation methods.

Image Processing

> The two most common examples are Local Frequency Estimation (LFE) and phase gradient (PG) methods. These methods measure the wavelength via image processing methods rather than solving the wave equation. There are even simpler versions of image processing based methods such as taking a linear profile across a wave image and measuring the wavelength and attenuation manually. Wave speed can be calculated from wavelength

knowing the mechanical frequency. Shear modulus would be density times square of wave speed. Basically all these methods based on the wave image itself without considering actual wave propagation, interference, inhomogeneity, anisotropy.

Direct Inversion of Wave Equation

These methods directly try to solve the wave equation under various assumptions. Depending in the type of wave displacement at hand, there can be variations of this method. Although this method is better at finding contours and small objects, it is very sensitive to noise, hence performs poorly under low SNR and requires accurate pre-filtering, which requires preliminary information about the wavelength to be estimated. But when these methods can be successfully applied, they can reveal the complex parameters in the wave equation, which image processing methods cannot.

Finite Element Modeling (FEM)

This method requires accurate information about geometry and boundary conditions prior to processing. Detailed image segmentation helps to construct a three-dimensional model of the target but precise boundary condition depends both on the actuation mechanism and other unknowns in the mechanical system. It may solve more complicated problems, but it may take too much time to solve the given problem, hence sometimes, it is unreasonable for clinical applications with the current computer technology.

CHAPTER 4

ULTIMATE MRE

The U-MRE method is a combination and generalization of two previously published methods, namely Spectral Displacement Projection (SDP) MRE (27) and Sampling Interval Modulation (SLIM) MRE (29). The SDP method allows multiple motion information at different frequencies and directions to be encoded at the same time. SLIM MRE, on the other hand, allows multiple motion information at the same frequency but in different directions to be encoded at the same time. U-MRE merges these two methods in the sense of maximum utilization of all frequency bins, hence filling up all signal space with the maximum information possible without increasing the total acquisition time. This means that, it is not possible to encode more information into signal space without sacrificing efficiency and/or SNR. There are alternative speed enhancements in the literature (11; 10); but, those are all at the cost of encoding efficiency.

In SDP MRE, provided that all MEG shapes are orthogonal for the duration of motion encoding, each frequency can be placed in their respective frequency bins. In order to avoid any overlap, frequencies and number of sampling points should be chosen accordingly. Depending on the frequencies and limitations on encoding duration, this method might end up with more time steps than the optimum number of time steps. For example for the frequencies 4, 5 and 6 kHz the minimum MEG time is 1 ms (to provide orthogonality) and the minimum sampling number is 14, in other words 14 time steps. On the other hand for the frequencies 1, 2 and 3 kHz we only need 8 time steps, while minimum MEG time is still 1 ms.

SLIM MRE utilizes an ambiguity, which originates from multiplication of frequency and phase difference between mechanical motion and MEG in the equation of total accumulated phase (Equation 3.10). A component of mechanical motion can be virtually shifted into any frequency bin. For example given 100 Hz mechanical motion, all read, phase and slice gradients are run at 100 Hz but their time shift amount with respect to mechanical frequency is different. The time shift of each MEG depends on which frequency component one wants to place the displacement information at that particular direction. Therefore, if one wants to place motion in the read direction into the first frequency bin corresponding to 100 Hz , motion in the phase direction into 200 Hz and motion in the slice direction into 300 Hz, time shifts with respect to mechanical motion should be 12.5 Hz, 25 Hz and 37.5 Hz, respectively for 8 time step case. Note that the minimum number of time steps should be chosen according to the number of directions to be encoded.

U-MRE combines the SDP and the SLIM MRE in the most general encoding scheme. In other words, U-MRE method allows one to capture n dimensional motion of m many mechanical motion frequencies without sacrificing any encoding efficiency with respect to classical MRE techniques given enough gradient strength and displacement.

4.1 Notation

As will be seen in the following sections, some of the notations related to time and frequency will become insufficient or ambiguous for advanced MRE methods. Therefore, an expanded set of notations will be presented. These new notations will clear any ambiguity that will emerge from generous usage of time and frequency terms in mathematics of conventional MRE.

$\mathbf{f_m}$	Mechanical Motion Frequency
$\mathbf{f_g}$	MEG Frequency
NoTS	Number of Time Steps
MEG Shape	An MEG function created to encode single motion information.
VTD	Virtual Time Domain
VFD	Virtual Frequency Domain
t	Time domain index
n	Virtual time domain index
f	Frequency domain index
$\boldsymbol{\alpha}$	Virtual frequency domain index

4.2 Phase Accumulation

Considering multiple mechanical frequencies and multiple gradient shapes encoding multiple directions for each frequency component, the conventional phase accumulation formula (Equation 3.9) can be extended as a summation of individual phase accumulation components, $\phi_{mv}(s)$.

$$\phi = \sum_{m=1}^{M} \sum_{v=1}^{V_m} \phi_{mv} \quad , \phi_{mv} = \Phi_{mv} \cos(2\pi f_m s_{mv} + \theta_{mv}), \tag{4.1}$$

where M is the total number of mechanical motion at different frequencies, m is the mechanical frequency index, V_m is the number of motion directions to be encoded for the m^{th} frequency and the the v is the index for direction. s_{mv} is the delay between mechanical motion of the m^{th} frequency and the gradient shape of the m^{th} frequency and the v^{th} direction for the n^{th} time step.

4.3 Sampled Phase Accumulation

In practice we can only measure $\phi_{mv}(s)$ for a finite number of s and from a mathematical point of view this process is no different than sampling of an analog signal. Therefore MRE wave images across different time offsets (in other words different s values) are actually time samples of wave propagation. The number of the samples is also called the number of time offsets in MRE literature. If we denote the sampling interval for the v^{th} direction of the m^{th} mechanical frequency as ΔT_{mv}, the sampled phase accumulation will be as follows,

$$\phi_{mv}[n] = \phi_{mv}(n\Delta T_{mv}) \tag{4.2}$$

In general, the timing of the sampling operation can be controlled for each motion information individually because we have the control of ΔT_{mv} via MEG programming (Appendix B). This allows us to acquire and arrange sampled time instances of each motion information independently. Since sampling time instances do not need to be consecutive and equally spaced in time, we will name this discrete domain (n) as the Virtual Time Domain (VTD) to avoid ambiguity with actual time domain (t).

4.4 Phase Accumulation in Frequency Domain

In order to separate different motion information, the sampled phase accumulation should be analyzed in the frequency domain. In this dissertation the discrete frequency domain is named the 'virtual frequency domain' (VFD) because the placement of information into frequency bins can be controlled by choice and not limited by the actual frequency of the sampled signal. This feature of MRE sampling can be possible because the sampling interval is multiplied by actual frequency (Equation 4.3). Therefore, the actual frequency can be multiplied or divided by the sampling interval ΔT_{mv} to change the location of that information in the virtual frequency domain.

$$\phi_{mv}[n] = \Phi_{mv} \cos\left(2\pi f_m \left(n\Delta T_{mv}\right) + \theta\right) \tag{4.3a}$$

$$\phi_{mv}[n] = \Phi_{mv} \cos\left(2\pi n (f_m \Delta T_{mv}) + \theta\right) \tag{4.3b}$$

In order to obtain VFD, a discrete Fourier transform is applied to the sampled phase accumulation in VTD. It is important to clarify that VFD is not directly related to the frequencies of mechanical motion or frequencies of MEG as VTD is not directly related to actual time domain.

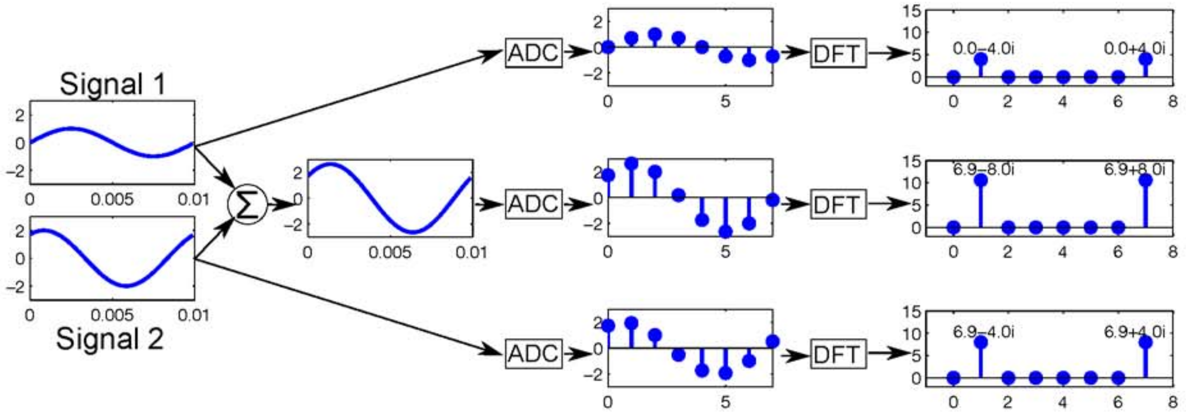

Figure 6: Analog signal sampling. Three discrete Fourier transforms (DFT) are presented on the right end of the figure. Top one is obtained after sampling of signal 1. Bottom one is obtained after sampling signal 2. Middle one is obtained after sampling linear addition of signal 1 and signal 2. It can be seen that middle DFT is also a linear summation of first and third DFTs.

4.5 Sampling Interval Modulation

The sampling process in MRE has some advantages over classic analog signal sampling. In classical analog sampling it is not possible to separate two signals with the same frequency when they are linearly combined (Figure 6), however, this is possible in MRE sampling .

When an analog signal composed of multiple information passes through an analog to digital converter (ADC), every information is sampled together at once. When the discrete Fourier Transform is obtained, it can be seen that two signals are merged into a single signal of one frequency. On the other hand, for MRE sampling, two signals with same frequency can be

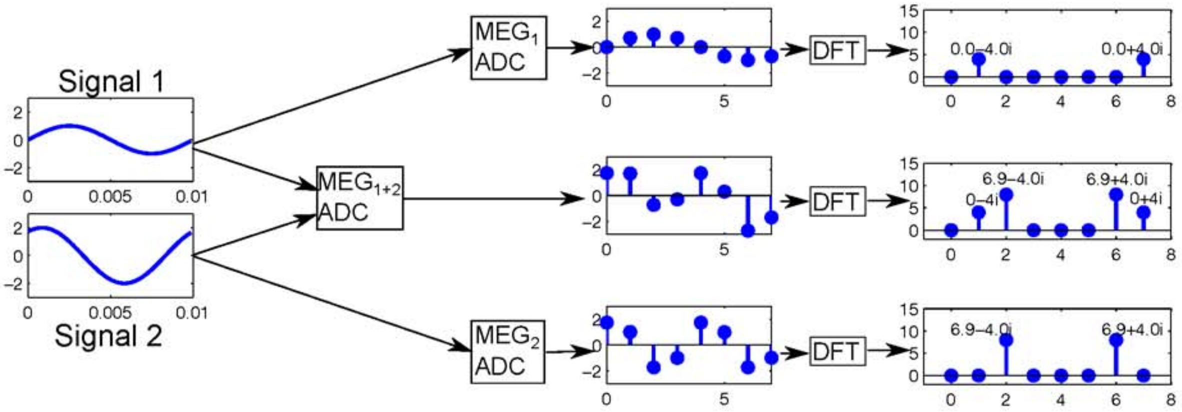

Figure 7: MRE Sampling. Three discrete Fourier transforms (DFT) are presented on the right end of the figure. Top one is obtained after sampling of signal 1. Bottom one is obtained after sampling signal 2 with a different rate than signal 1. Middle one is obtained after simultaneously sampling signal 1 and signal 2 with different sampling rates. It can be seen that middle DFT is also a linear summation of first and third DFTs.

sampled independently as long as they have different vibration directions. This is possible because each MEG shape will encode one information and each MEG shape can be programmed independently. Although the acquired data will be the summation of sampled wave information, they can be separated in VFD.

Sampled form of general phase accumulation (Equation 4.1) is shown in (Equation 4.4)

$$\phi[n] = \sum_{m=1}^{M} \sum_{v=1}^{V_m} \phi_{mv}[n]. \tag{4.4}$$

where m is the mechanical frequency index, v is the gradient shape index, M is the total number of frequencies, V_m is the total number of gradient shapes for the m^{th} frequency component, n is the time step and $\phi_{mv}[n]$ is the phase accumulation due to gradient shape g_{mv}. For a given m all gradient shapes have different directions, therefore the index v can also be addressed as a direction index of gradient shapes for the m^{th} frequency. The phase accumulation created by individual gradient shapes is the integration of the projection of mechanical displacements on that particular gradient vector multiplied by gyromagnetic ratio is given in (Equation 4.5).

$$\phi_{mv}[n] = \gamma \int \mathbf{g}_{mv}(n,t) \cdot \mathbf{u}_m(t) dt, \tag{4.5}$$

where γ is the gyro magnetic ratio, $\mathbf{g}_{mv}$ (Equation 4.6) is the gradient shape for the m^{th} frequency in the v^{th} direction and $\mathbf{u}_m$ is the mechanical motion vector of the m^{th} frequency.

$$\mathbf{g}_{mv}\left(n\right) = \begin{cases} G_{mv} \sin\left(2\pi f_m t - \theta_{mv}\left(n\right)\right) \hat{\mathbf{e}}_{mv}, & s_{mv}(n) < t < s_{mv}(n) + T \\ \\ 0, & \text{otherwise} \end{cases} \tag{4.6}$$

The piecewise continues gradient shape function given in (Equation 4.6) avoids any discontinuity in gradient shapes given that $s_{mv}(n) = \theta_{mv}(n)/(2\pi f_m)$ and $T = k/f_m$, where $k \in \mathbb{Z}^+$. The amplitude of the gradient shape g_{mv} is denoted by G_{mv}, which is a real valued scalar. This study does not cover 1^{st} moment nulling techniques, therefore the gradient shapes are designed to start from 0° phase as can be seen from the limits given in (Equation 4.7).

$$\mathbf{g}_{mv}\left(n\right) = \begin{cases} G_{mv} \sin\left(2\pi f_m \left(t - s_{mv}(n)\right)\right) \hat{\mathbf{e}}_{mv}, & s_{mv}(n) < t < s_{mv}(n) + T \\ \\ 0, & \text{otherwise} \end{cases} \tag{4.7}$$

The displacement vector field in the subject due to mechanical motion is broken down into individual frequency components (Equation 4.8) indexed by m

$$\mathbf{u}_m(t) = U_m \sin\left(2\pi f_m t + \psi_m\right) \hat{\mathbf{e}}_m, \tag{4.8}$$

where U_m is a real valued scalar indicating the amplitude of the m^{th} mechanical motion for the given pixel, ψ_m is the phase of the mechanical motion relative to $t = 0$ and $\hat{\mathbf{e}}_m$ is the unit vector for the direction of the m^{th} mechanical motion. Please note that although ψ_m is eventually the source of the wave image pattern, it doesn't play a role in formulation of U-MRE pulse sequence.

All the derivations were done pixel wise because the spatial dimension is independent of all the parameters used in this section, other than the phase and the amplitude of mechanical motion at a particular pixel, which are $\psi_m(t, \mathbf{r})$ and $U_m(\mathbf{r})$ respectively. Therefore, the spatial dependencies of U_m and ψ_m are omitted in the derivations.

4.6 Frequency Bin Placement

Since we are assuming all mechanical motions and gradient shapes are composed of linear combinations of harmonic functions, it is possible to work with complex exponential forms of signals rather than taking discrete Fourier transforms. If a harmonic signal $a(t)$ is sampled at N points over b many periods it can be expressed as follows in discrete domain,

$$a[n] = real\left\{e^{j2\pi\frac{n}{N}b}\right\} \quad ,n \in \{0, ..., N-1\} \tag{4.9}$$

This signal would fall into the b^{th} frequency bin if a discrete Fourier transform is taken. Please note that there would be another complex conjugate component due to the symmetry of the frequency domain but the complex conjugate symmetric part of signals are of no use in the context of this dissertation. Therefore, we will only use first $\frac{N}{2}$ (N is even) or $\frac{N-1}{2}$ (N is odd) frequency bins and ignore the complex conjugate symmetric part of frequency domain.

If we rewrite (Equation 4.3) in complex exponential form,

$$\phi_{mv}[n] = \Phi_{mv}\cos(2\pi f_m \Delta T_{mv} n + \theta) \tag{4.10a}$$

$$= \Phi_{mv} real\left\{e^{-j(2\pi f_m \Delta T_{mv} n + \theta)}\right\} \tag{4.10b}$$

and place $\phi_{mv}[n]$ into the b^{th} frequency bin, (Equation 4.10) should be solved for ΔT_{mv} using (Equation 4.9) as follows,

$$e^{-j(2\pi f_m \Delta T_{mv} n+\theta)} = e^{-j(2\pi \frac{n}{N} b+\theta)} \tag{4.11a}$$

$$n f_m \Delta T_{mv} = \frac{n}{N} b \tag{4.11b}$$

$$\Delta T_{mv} = \frac{b}{N f_m} \tag{4.11c}$$

The start time of a particular gradient shape, $s_{mv}(n)$ (Equation 4.7), is the variable in our control while programming the gradient shapes. Therefore, $s_{mv}(n)$ can be derived using calculated ΔT_{mv} as follows,

$$s_{mv}(n) = \frac{\theta_{mv}(n)}{2\pi f_m} \quad , \theta_{mv}(n) = ((n-1)\Delta T_{mv})\, 2\pi f_m \quad , \Delta T_{mv} = \frac{b}{N f_m} \tag{4.12a}$$

$$s_{mv}(n) = b\left(\frac{n-1}{N}\right)\frac{1}{f_m}, \tag{4.12b}$$

where b is the frequency bin , N is the number of time steps (NoTS) and f_m is the frequency of mechanical motion.

This completes the derivation of a gradient shape (Equation 4.7), which encodes the v^{th} direction component of the m^{th} mechanical frequency into the b^{th} frequency bin via adjusting the start time, $s_{mv}(n)$, and thus the time shift, $\Delta T_{mv}(n)$ of a gradient shape for each time step.

CHAPTER 5

METHODS

5.1 Experimental Setup

This study was conducted using a 500 MHz (11.74 Tesla) vertical bore Bruker(ID = 56 mm) micro imaging MRI system. A saddle RF coil (ID = 12mm) and micro imaging gradient coils (ID 19 mm) were used. Maximum gradient strength per coil was 300 Gauss per cm. The sample was oscillated into harmonic motion by a piezo ceramic stack that provides 11.6 μm displacement at 100 volts(6.5 x 6.5 x 18 mm, Thor Labs Inc). A counter mass was placed on the other side of the Piezo stack in order to reduce recoil by providing inertial ground (Figure 8). The Piezo stack was driven by an audio power amplifier (P3500S Power Amplifier, Yamaha Corporation of America, Buena Park, CA). The power amplifier is driven by a function generator (33220A Function / Arbitrary Waveform Generator, 20 MHz, Agilent Technologies Test and Measurement, Englewood, CO), which was triggered from the MRI system. The output of the audio power amplifier is biased by a DC power supply (E3634A 200W Power Supply, Agilent Technologies Test and Measurement, Englewood, CO) in order to prevent a negative voltage at the terminals of the piezo stack. A negative voltage potential in the piezo stack may create more non-linear motion while degrading the performance of piezo stack in time.

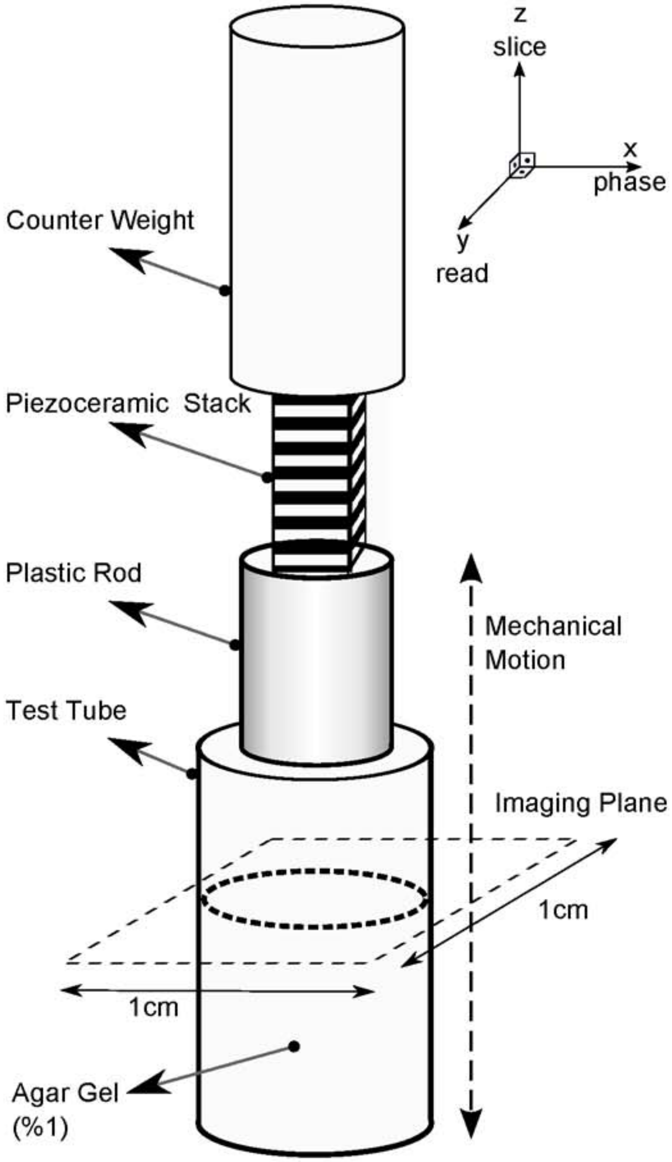

Figure 8: Diagram of the mechanical setup.

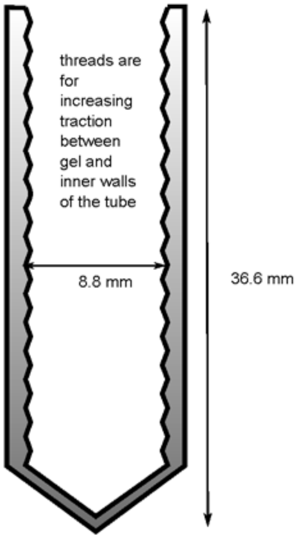

Figure 9: Plastic tube threaded inside to provide better traction between water based agarose gel and the inner walls of plastic tube.

5.2 Sample Preparation

The sample was % 1 SeaKem®LE Agarose gel (Rockland, ME, USA) and % 99 water by weight. Water boiled then the agarose in powder form added to the boiling water, while stirring it with magnetic stir bars. Once the agarose powder melted, which takes less than a minute, it was poured in the plastic sample tube and let cool down to room temperature. Sample was freshly prepared and scanned at the same day. The sample tube was threaded to provide firm contact between agarose gel and the tube (Figure 9). Due to comparable size of threads (0.5 mm apart, 05 mm deep) and wave lengths of the mechanical motion at frequencies experiment conducted, it was possible to observe wave motion in all three spatial dimensions.

5.3 Image Acquisition

A gradient echo based MRE pulse sequence was used in this experiments. The signal generator was triggered before the RF pulse, therefore the displacement vector field reaches steady state harmonic mechanical motion by the time MEGs begin motion encoding. Six axial slices of thickness 1 mm were acquired with 128 x 128 resolution over 1 cm x 1 cm field of view. The flip angle was 30 degrees (check this) and the echo time (TE) was 3.95 ms plus the duration of longest MEG. Some of the scans were completed with 4 time steps while others used 8 or 20 time steps depending on the experiment. Also, all scans were repeated with inverse polarization of MEGs and the resultant images were divided (this will subtract phase components since the resultant images are complex valued) to each other to eliminate any common phase artifact and bias originating from anything other than MEGs.

5.4 Motion Encoding

Motion encoding gradients need to have sinusoidal shape to avoid encoding higher harmonics of mechanical motion, which will be generated due to the non-linear nature of mechanical actuators. The most common cause of for non-linearity would be due to clipping or non-symmetric behavior of actuator motion. On top of that it is expected to have non-linearity in tissue mechanics (41). Hence, although the trapezoidal MEG shape is common across MRE experiments because of its higher motion encoding efficiency, we would not suggest using any shape other than sinusoidal. Please note that the above discussion doesn't exclude windowing. It is naturally expected to obtain better results with windowing via better frequency and dynamic response of gradient coils. For simplicity, we didn't use any windowing function over the gradient shapes. Depending on the number of information to be acquired, that many gradient shapes should be created and distributed across the gradient coils based on the direction of component of motion. Each gradient shape should have its own frequency, duration and time offset values. Each gradient coil may have a linear combination as many gradient shapes as needed. The frequency of each gradient shape should match the frequency of motion to be encoded. The duration and time offset values for each gradient shape is explained in the Unified sampLing Time Interval ModulATion section. A generic C language code for creating ULTIMATe MRE gradient shapes is given in Appendix B.

5.5 Reconstruction

Acquired k-space data was reconstructed into complex images off-line using a commercial software package (MATLAB 8.1, The MathWorks Inc., Natick, MA, 2013). Each image is divided by its inverse polarized MEG reciprocal to eliminate common phase artifacts. Depending on time step number 4, 8 or 20 snapshots of wave propagation were obtained throughout the time. In this study 4, 8 or 20 analytical wave images were obtained in Virtual Frequency Domain (VFD) depending on the time step number. This number can be any value as long it allows enough empty frequency bins in the VFD for the information to be encoded (Figure 10). Experiment parameters were adjusted such that each frequency bin contains harmonic displacement information of one frequency in one particular direction. In other words each frequency bin in VFD contains single information, which cannot be resolved into independent components in terms of frequency and/or direction.

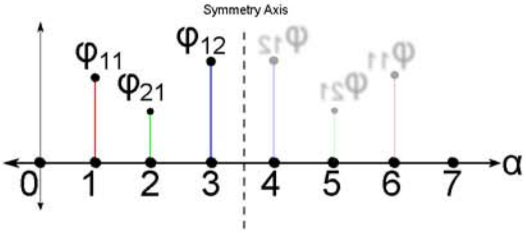

Figure 10: Population of frequency bins in Virtual Frequency Domain (VFD). In this example there are three different information: ϕ_{11} and ϕ_{12} belong to two different directions for the first frequency and ϕ_{21} belongs to one direction at the second frequency component.

CHAPTER 6

RESULTS

6.1 Encoding Multiple Frequencies in Single Direction

Three frequencies (5000 Hz, 6000 Hz and 7000 Hz) were encoded for a single direction, slice direction, of an axial imaging slice. This process was done in two different ways. In the first one, they were encoded individually as in conventional MRE (First row in Figure 11). In the second way, they were encoded all at once, using ULTIMATe MRE (Second row in Figure 11). Both methods had 8 time steps. Each gradient shape uses 25 % of the maximum gradient power. This means that, in conventional MRE the maximum level of total MEG does not get higher than 25 % at a given time, while in ULTIMATe MRE, it reaches up to 75 % at some time instances, when the gradient shapes add up (Figure 19).

6.2 Encoding Multiple Frequencies in Multiple Directions

The performances of conventional MRE and ULTIMATe MRE were investigated for multiple frequencies and multiple directions. For conventional MRE, 4 time steps have been used except for slice direction encoding where both 4 time steps and 8 time steps were used. For ULTIMATe MRE four different cases were investigated. The first one was 8 time step SDP MRE where different frequencies for the three directions were encoded at once, in other words, one frequency per direction. So there were a total of 3 SDP scans to cover all three directions at three frequencies. The second one was 8 time step SLIM MRE where three directions for the same

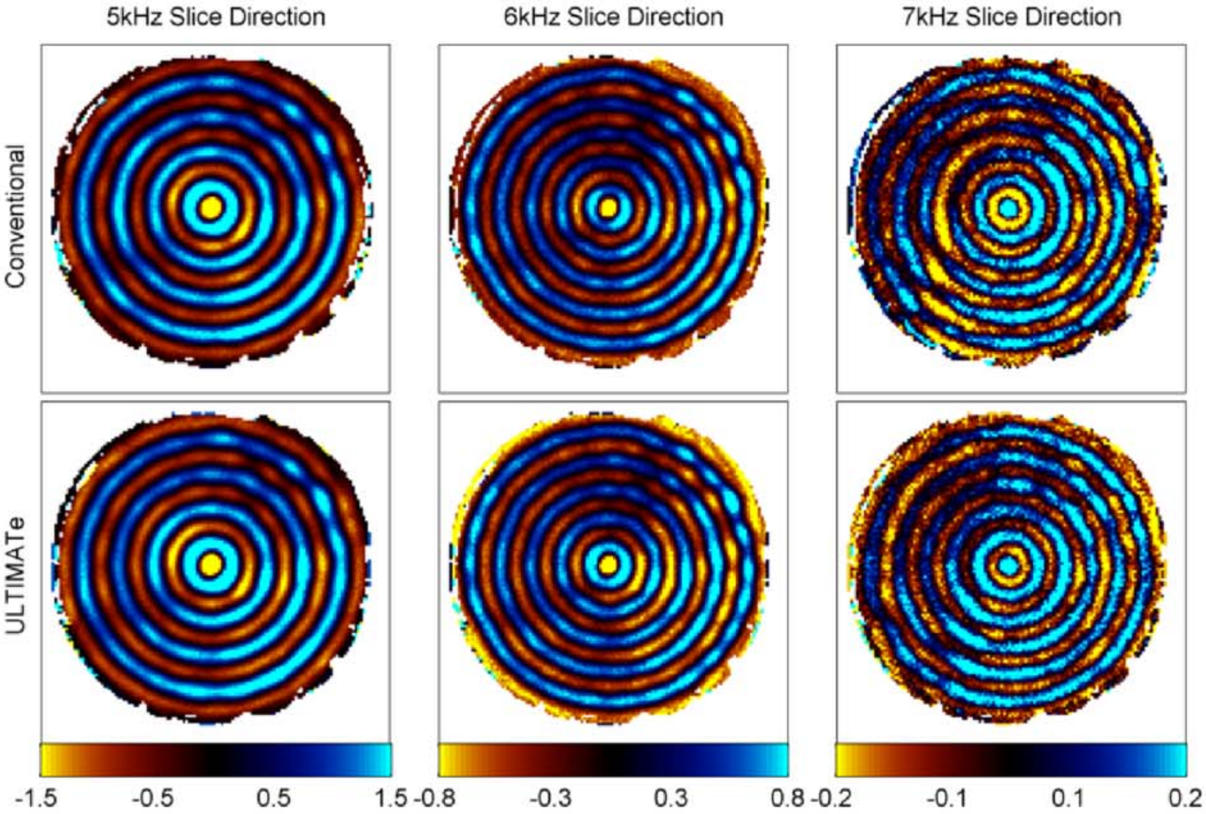

Figure 11: Two sets of MRE scans conducted on a cylindrical agarose gel sample. The goal was to capture the slice direction component of the harmonic wave propagation of three different frequencies of an axial image. First row shows wave images of conventional MRE. Second row shows wave images of ULTIMATe MRE. The three wave image in the first row required three separate scans while the three wave images in second row were acquired in one scan.

frequency encoded at once. For SLIM MRE, as in the case of SDP MRE, a total of 3 scans were used to cover all three directions at three frequencies. The third one was 8 time step ULTIMATe MRE, where three frequencies were encoded for one direction at a time. As in the previous two cases, a total all of three scans were needed to cover all three directions. The last one is 20 time step ULTIMATe MRE, where all three directions and all three frequencies were encoded at once in a single scan.

TABLE I: Time Comparison of MRE methods

Method	Time Steps	Scans	Wave Images	Phase Images
MRE	4	9	4x9=36	72
MRE	8	9	8x9=72	144
SDP	8	3	8x3=24	48
SLIM	8	3	8x3=24	48
U-MRE	8	3	8x3=24	48
U-MRE	20	1	20x1=20	40

6.3 Stiffness Estimations

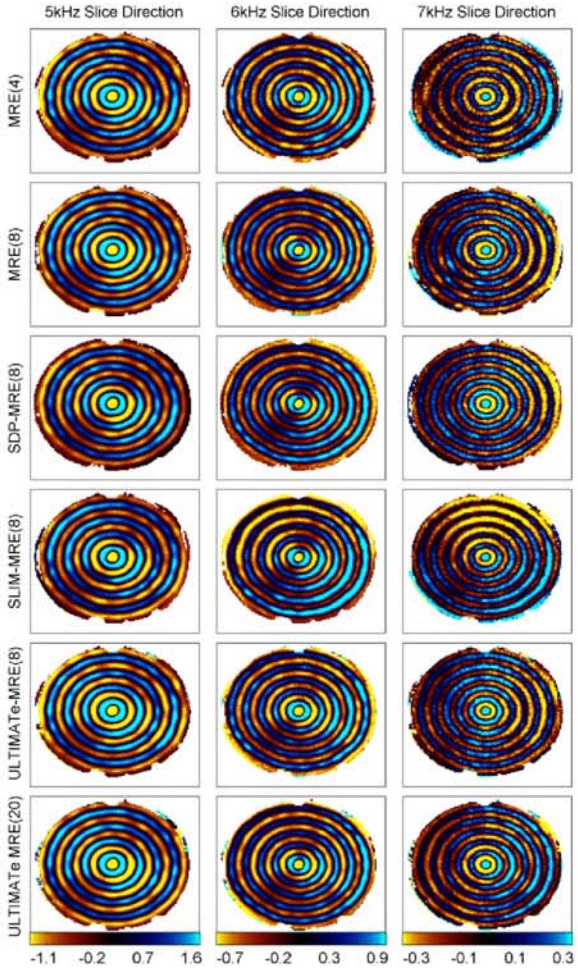

Figure 12: Six sets of MRE scans conducted on a cylindrical agarose gel sample. The goal was to capture wave propagation at three different frequencies in the slice direction of an axial image. First row shows wave images of conventional MRE of four time steps. Second row shows wave images of conventional MRE of eight time steps. Third row shows wave images of SDP MRE of eight time steps. Fourth row shows wave images of SLIM MRE of eight time steps. Fifth row shows wave images of ULTIMATe MRE of eight time steps. Sixth row shows wave images of ULTIMATe MRE of twenty time steps. The three wave image in the first row required three separate scans while three wave images in second row acquired at one scan.

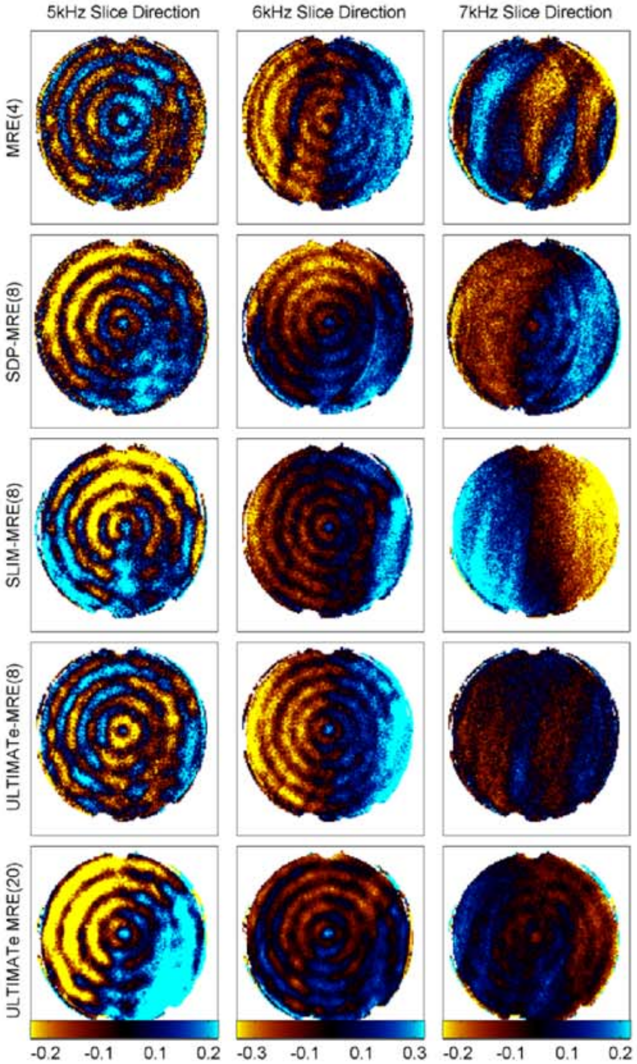

Figure 13: Six sets of MRE scans conducted on a cylindrical agarose gel sample. The goal was to capture wave propagation at three different frequencies in the phase direction of an axial image. First row shows wave images of conventional MRE of four time steps. Second row shows wave images of SDP MRE of eight time steps. Third row shows wave images of SLIM MRE of eight time steps. Fourth row shows wave images of ULTIMATe MRE of eight time steps. Fifth row shows wave images of ULTIMATe MRE of twenty time steps.

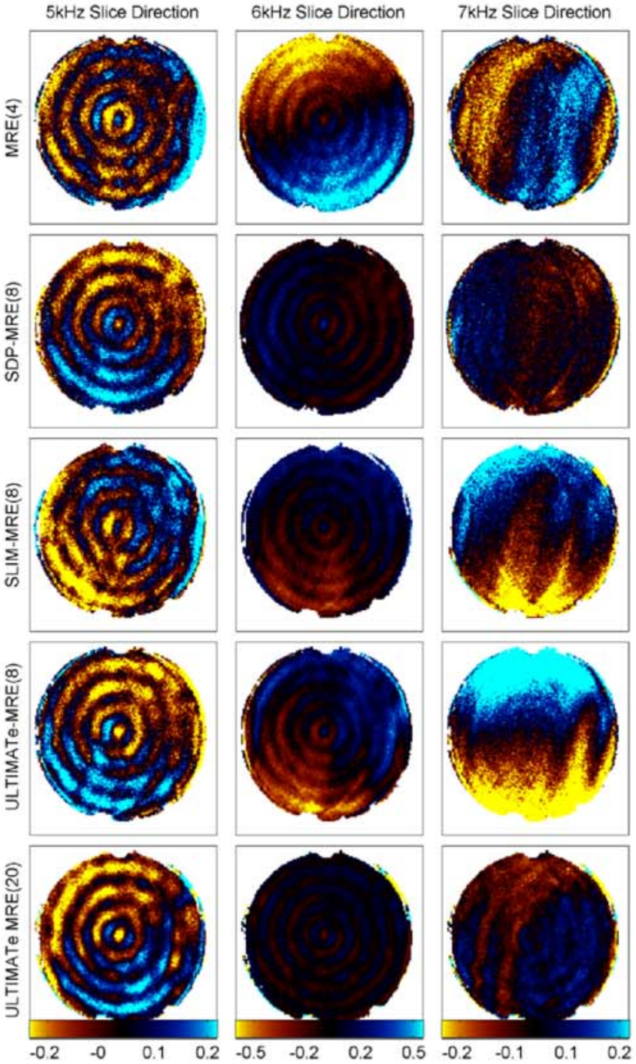

Figure 14: Six sets of MRE scans conducted on a cylindrical agarose gel sample. The goal was to capture wave propagation at three different frequencies in the read direction of an axial image. First row shows wave images of conventional MRE of four time steps. Second row shows wave images of SDP MRE of eight time steps. Third row shows wave images of SLIM MRE of eight time steps. Fourth row shows wave images of ULTIMATe MRE of eight time steps. Fifth row shows wave images of ULTIMATe MRE of twenty time steps.

TABLE II: Motion Information Encoding Comparison of MRE Methods

Method	Time Step	$\frac{\text{Direction}}{\text{Scan}}$	$\frac{\text{Frequency}}{\text{Scan}}$	$\frac{\text{Frequency}}{\text{Direction}}$	$\frac{\text{Direction}}{\text{Frequency}}$	$\frac{\text{Information}}{\text{Scan}}$
MRE	4	1	1	1	1	1
MRE	8	1	1	1	1	1
SDP	8	3	3	1	1	3
SLIM	8	3	1	1	3	3
U-MRE	8	1	3	3	1	3
U-MRE	20	3	3	3	3	9

TABLE III: Information Encoding Map of MRE Methods

Method	5000 Hz			6000 Hz			7000 Hz		
	read	phase	slice	read	phase	slice	read	phase	slice
MRE	●								
MRE		●							
MRE			●						
MRE				●					
MRE					●				
MRE						●			
MRE							●		
MRE								●	
MRE									●
SDP	●				●				●
SDP		●				●	●		
SDP			●	●				●	
SLIM	●	●	●						
SLIM				●	●	●			
SLIM							●	●	●
U-MRE(8)	●			●			●		
U-MRE(8)		●			●			●	
U-MRE(8)			●			●			●
U-MRE(20)	●	●	●	●	●	●	●	●	●

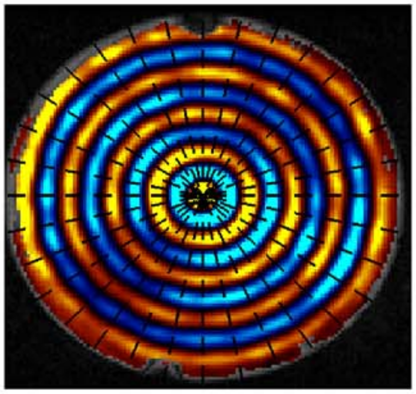

Figure 15: Linear profiles of complex wave image taken passing through the center of tube. A total of 36 linear profiles were taken for each slice, frequency and MRE method. In this figure, to avoid clutter only 16 linear profiles are shown indicated by dashed lines.

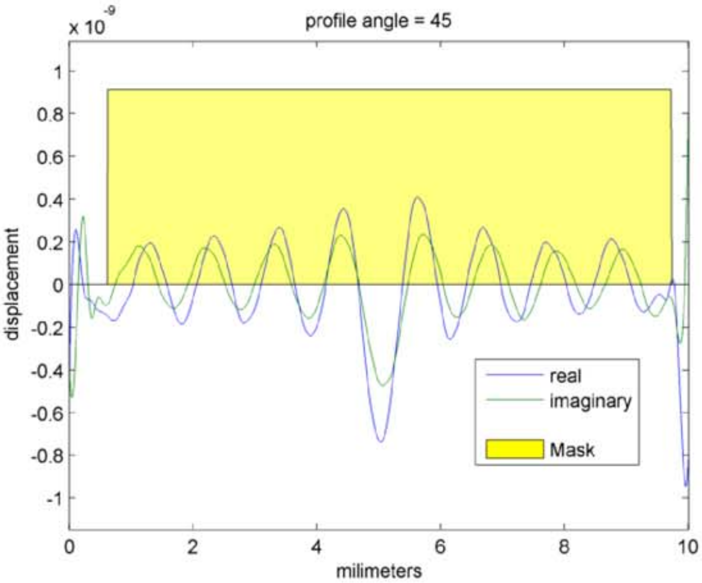

Figure 16: Linear profile of complex wave image (analytical wave propagation image) at 45 degree angle shown in Figure 15 . Real and imaginary parts of the wave image were plotted in blue and green color respectively. Yellow shaded area indicates the masked part. The region outside the mask was discarded in stiffness estimation calculations.

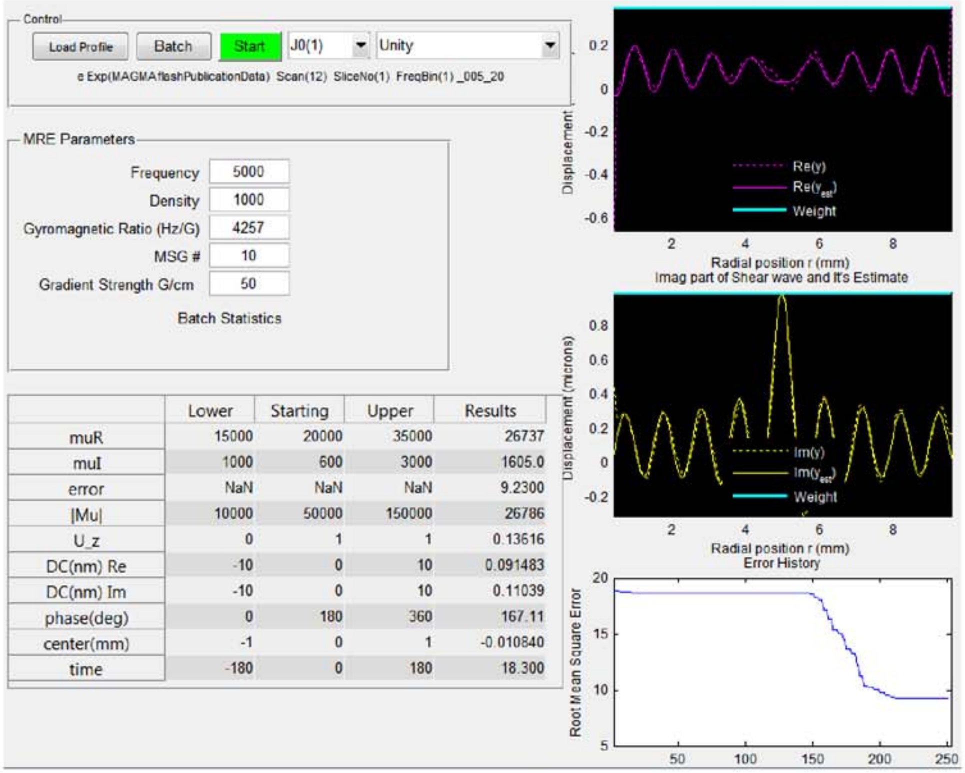

e Exp(MAGMAflashPublicationData) Scan(12) SliceNo(1) FreqBin(1) _005_20

Frequency: 5000
Density: 1000
Gyromagnetic Ratio (Hz/G): 4257
MSG #: 10
Gradient Strength G/cm: 50

	Lower	Starting	Upper	Results
muR	15000	20000	35000	26737
muI	1000	600	3000	1605.0
error	NaN	NaN	NaN	9.2300
|Mu|	10000	50000	150000	26786
U_z	0	1	1	0.13616
DC(nm) Re	-10	0	10	0.091483
DC(nm) Im	-10	0	10	0.11039
phase(deg)	0	180	360	167.11
center(mm)	-1	0	1	-0.010840
time	-180	0	180	18.300

Figure 17: Complex linear profile taken in Figure 16 was fitted in to analytical solution of cylindrical wave propagation. Real and Imaginary parts of shear modulus μ can be estimated given the density of the material and the mechanical frequency. Purple lines on the top right figure show the real part of complex wave image profile and yellow lines in the figure below show the imaginary part of complex wave image. Dashed lines are used for experimental data and solid lines are used for wave propagation calculated with estimated μ. Blue line in the bottom figure indicates the decreasing error estimation throughout the iterations. The table contains the lower and upper boundaries, starting points and final estimations of parameters estimated for curve fitting operation.

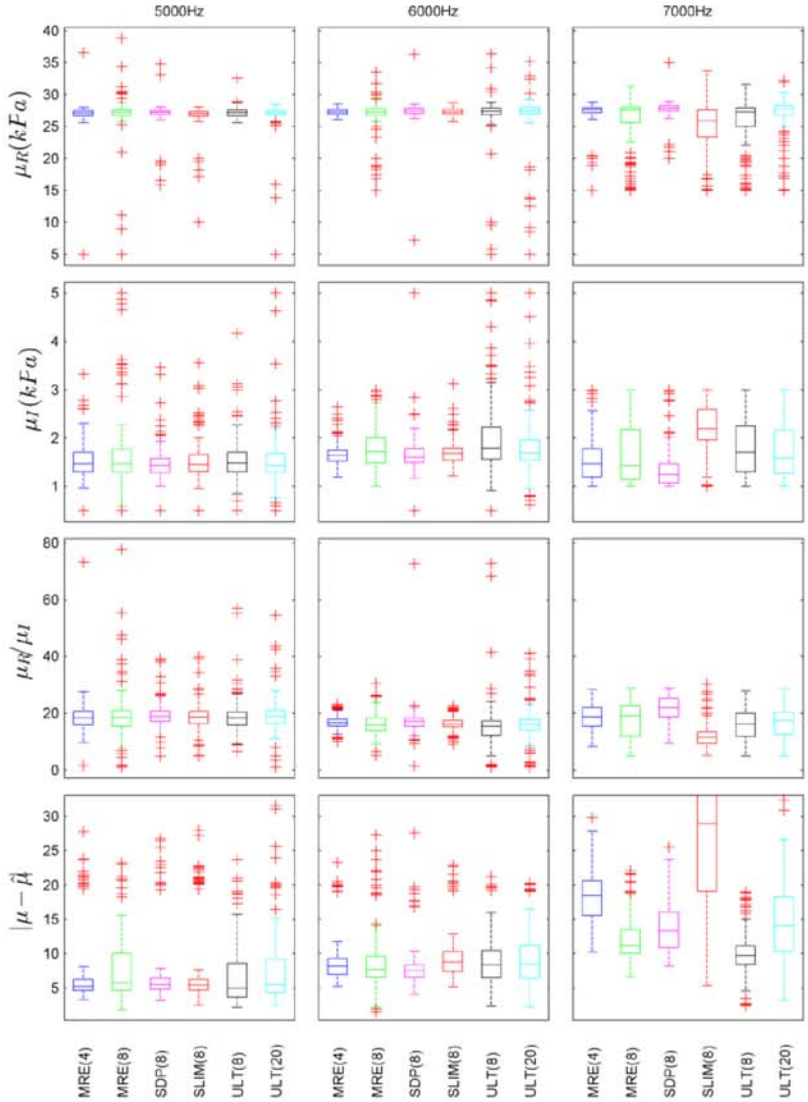

Figure 18: Shear modulus μ was estimated for three different frequencies: 5 kHz, 6 kHz and 7 kHz. Two main types of encoding methods were used. The first one is conventional MRE and the second one is ULTIMATe MRE. There were two cases for conventional MRE, 4 time steps and 8 time steps. There were 4 cases of ULTIMATe MRE, 8 time step SDP-MRE, 8 time step SLIM-MRE, 8 time step ULTIMATe MRE and 20 time step ULTIMATe MRE. Note that SDP and SLIM MRE are special cases for ULTIMATe MRE, where maximum gradient power in one direction can be achieved.

CHAPTER 7

DISCUSSION

7.1 Speed Enhancements

Given the N time steps, conventional MRE yields only one analytical wave image. In ULTIMATe MRE and its special cases, such as SDP and SLIM, the number analytical wave images increases with increasing number of N (Equation 7.1). If we define speed efficiency as the number of wave images per MRE scan, in Table IV we can compare the time efficiencies for conventional MRE and ULTIMATe MRE for $N = 4, 8, 16, 20$ and $N \to \infty$.

$$\text{Number of Wave Images for Conventional MRE} = 1, \qquad N \in (\mathbb{Z}^+) \tag{7.1a}$$

$$\text{Number of Wave Images for ULTIMATe MRE} = \begin{cases} \frac{N}{2} - 1, & N \in \text{even}(\mathbb{Z}^+) \\ \frac{N+1}{2} - 1, & N \in \text{odd}(\mathbb{Z}^+) \end{cases} \tag{7.1b}$$

7.2 Stiffness Estimation Performances

In this study the performance of different pulse sequences were compared using a robust method developed in (8). Since the sample was a uniform gel in axi-symmetric motion in a cylindrical tube, a closed form solution of the shear modulus estimation exists. We did not use other well known methods such as direct inversion or local frequency estimation because direct inversion suffers greatly from its assumptions that are not satisfied and the local frequency estimation algorithm can only provide shear stiffness values, which is just an output of the image processing method rather than a wave equation related parameter.

In the method defined in (8), linear profiles passing through the center of the test tube, are fitted to the closed form solution of the wave propagation. This fitting is done by optimizing curve parameters by minimizing mean square error between the estimated curve and the actual wave profile. Although there are more parameters than the shear modulus, we present the shear modulus estimation in this study since the rest of the parameters are related to geometric and time offsets needed for compensating errors introduced while taking linear profiles.

For 5 kHz and 6 kHZ the real and imaginary parts of shear modulus yields almost the same results for the median and distribution with different outliers. The difference we believe comes from the error from linear profiles because the center of the tube was aligned manually. So it is expected to have few pixels shift in the selection of center of the cross section of the tube for each scan. The 7 kHz results do not match as well as the 5 kHz and 6 kHZ; but, considering the lower SNR due to higher attenuation at higher frequencies estimated values are still very close.

Hence, although ULTIMATe MRE and it derivatives end up with less SNR than conventional MRE, this does not affect the performance of stiffness estimation. Therefore, conventional MRE scans can be replaced with ULTIMATe MRE scans to reduce total acquisition time without sacrificing stiffness estimation accuracy.

7.3 Limitations

Depending on the configuration of frequencies and directions to be encoded ULTIMATe MRE may introduce some limitations to the amount of motion encoding. These limitations cause less phase accumulation and less phase to signal ratio, which would affect the performance of stiffness estimation algorithm (11). We can categorize these limitations under four titles. The first one is Gradient coil power distribution. This would be an issue when there is more than one gradient shape per gradient coil. The second one is multiple frequency excitation of the mechanical actuator. As the name implies, when there is more than one frequency to be encoded at the same time, they need to be introduced from the same actuator with limited output capability. The third one is increased echo time. In the case of encoding of a frequency in more than one direction, an increase in echo time is inevitable, although there are ways to keep this at minimum. And there are other issues with operating multiple gradients at the same time and driving them at higher powers and higher frequencies.

7.3.1 Gradient Power Distribution

There is a limit on the magnetic field strength that gradient coils can generate. When we are using multiple gradient shapes on one gradient coil, these shapes add up to a maximum level at some point in time and this level cannot be larger than the gradient coil amplifier limit. Therefore, amplitudes of each gradient shape must be adjusted such that, summation should be under an upper limit. This will result in less phase encoding per frequency compared to single frequency encoding. Although there is no way around this problem, other than accepting clipping of gradient shapes (Figure 19), which will introduce unexpected encoding distortion and degrades the phase to noise ratio, we can distribute the amplitudes of gradient shape so that we would have a uniform phase encoding performance for each frequency. Most of the time higher frequencies will attenuate faster, so it would be more efficient to reserve a larger portion of the gradient strength for higher frequencies to compensate lower displacement amplitudes at higher frequencies.

7.3.2 Multiple Frequency on Mechanical Actuator

Similar to the previous section, the mechanical actuator also has a finite displacement limit. If that limit is reached, displacement will be clipped and it will introduce harmonics of input frequencies, which will eventually contaminate the spectrum.

The solution to this problem, as in the previous section, is reserving more power for higher frequencies that in return would distribute the phase accumulation more uniformly in the phase image. But we are just not limited to this solution in the mechanical actuator case. Although it is very difficult to introduce a new set of gradients for each frequency, it is quite easy to use different actuators for different frequencies as long as the space in the RF coil permits.

Depending on the actuator type, it would be possible to place different actuators inside the imaging area. This is especially feasible in pneumatic applications while, not so easy for piezo stack or rod-based actuators.

7.3.3 Implications on Echo Time (TE)

In MRE, the duration of MEGs placed in the pulse sequence adds upto the echo time. Shifting the MEG with respect to mechanical motion can be achieved by shifting the mechanical motion itself, shifting the start instance of pulse sequence or both. But this trick is not viable

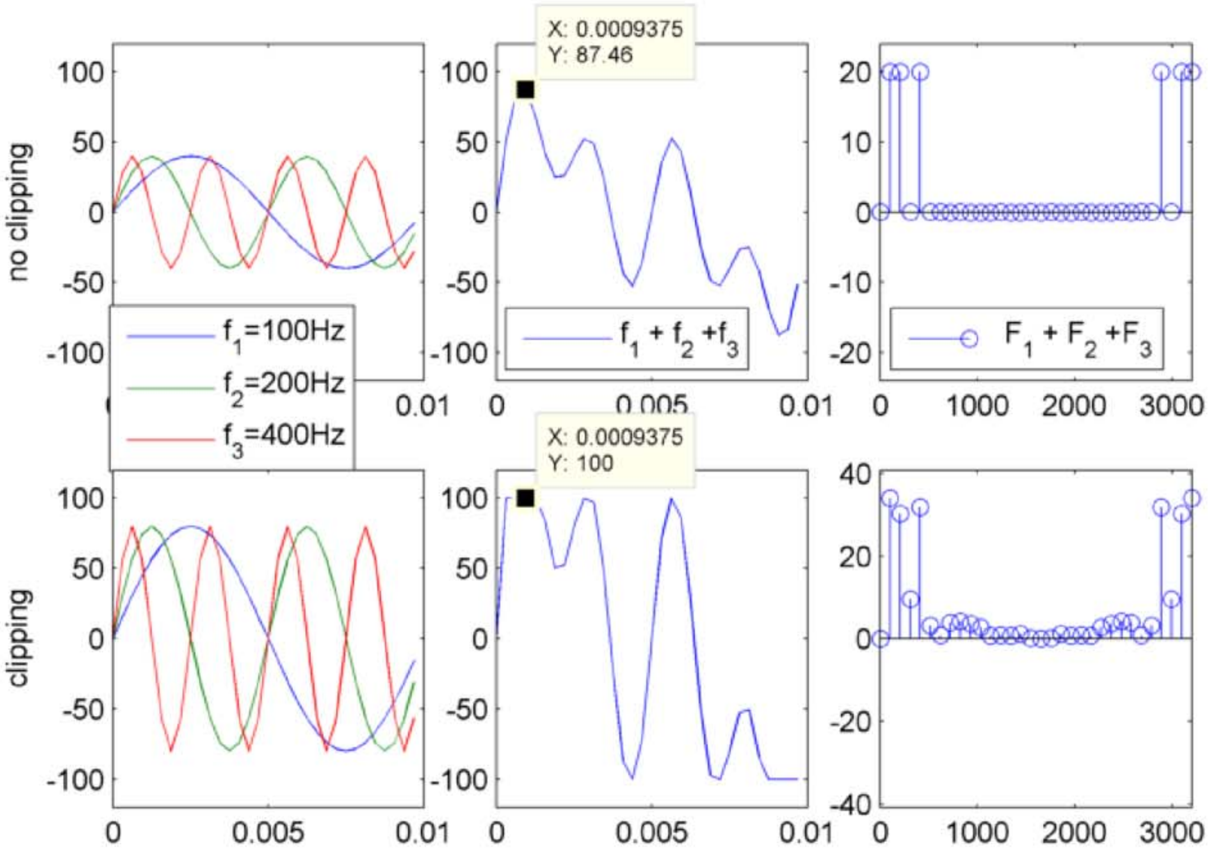

Figure 19: Two cases of a MEG function are presented in this figure. First row is combination of three MEG shapes of frequencies 100 Hz, 200 Hz and 400 Hz. Amplitudes of all of them are between -% 40 and +% 40. Second row has the same shape functions, but the amplitudes span from -% 80 and +% 80. In the first column, individual gradient shape functions, and in the second column summation of those gradient shapes are presented. Note that, in the second row since summation of amplitudes are greater than % 100, they are clipped at that limit. Last column shows the frequency spectrum of the summation of gradient shapes. While there are three distinct impulses in the first row, the second row has problems such that power of individual shapes are distributed across the spectrum due to clipping.

anymore for ULTIMATe MRE. To be more exact, it is not applicable if a frequency needs to be encoded for more than one direction.

If we consider SLIM MRE, three directions are encoded for a single frequency and each MEG shape should be shifted with respect to mechanical motion by different amounts. This is not possible by simply shifting the mechanical motion, the MEGs themselves should also be shifted with respect to each other. This shifting would introduce an extra increase in echo time on top of the MEG duration. This may create a significant SNR decrease if not taken care of carefully.

Fortunately, since the signals we are encoding are steady state harmonic motions and gradient shapes themselves are harmonic functions, we can utilize symmetry of phase shifts to minimize the TE increase along with controlling the phase of mechanical motion.

In Table V a standard example of SLIM MRE is given, where one frequency is encoded for three directions. Each gradient shape has it's own phase shift $\theta_i, i \in \{1, 2, 3\}$. For each time step n the required phase shift, modulo 2π and modulo π is given. We can take modulo π due to the fact that π phase shift is just multiplying the result of 0 phase shift by -1. The minimum of these three phase shift can be subtracted from the phase of the mechanical motion and that leaves the last three rows, which are the minimum required phase shifts for three gradient shapes. As can be seen from last three rows, in the worst case scenario only $\pi/2$ phase shift is necessary.

However, SDP type ULTIMATe MRE methods (single direction per frequency) are not affected by this issue since the phase of each frequency can be shifted from the signal generator itself while keeping the MEG phases constant with respect to pulse sequence.

7.3.4 Other Drawbacks

7.3.4.1 Concomitant Fields

When a linearly changing gradient field is applied, concomitant magnetic fields occur with non-linear special dependence (42). This is because of Maxwell's equation where the divergence of a magnetic field has to be zero. On top of this whenever a Z gradient runs along with an X and/or a Y gradient, cross terms occurs (Equation 7.2).

$$B_C\{x,y,z,t\} = \frac{1}{2B_0}\left\{\left(G_x z - \frac{G_z x}{2}\right)^2 + \left(G_y z - \frac{G_z y}{2}\right)^2\right\} \tag{7.2a}$$

$$B_C\{x,y,z,t\} = \frac{1}{2B_0}\left\{G_x^2 z^2 + G_y^2 z^2 + \frac{G_z^2\left(x^2+y^2\right)}{4} - G_x G_z z x - G_y G_z z y\right\}, \tag{7.2b}$$

where B_C is the concomitant field function of spatial variables x, y, z and time variable, t. B_0 is the main magnetic field and G_x, G_y, G_z are the gradient field strengths of x, y and z gradient coils, respectively.

Since in an MRE application it is desirable to have maximum available gradient power to achieve maximum encoding efficiency, concomitant fields would be introduced more than most of other imaging methods. However, if we compare the strength of these unwanted concomitant

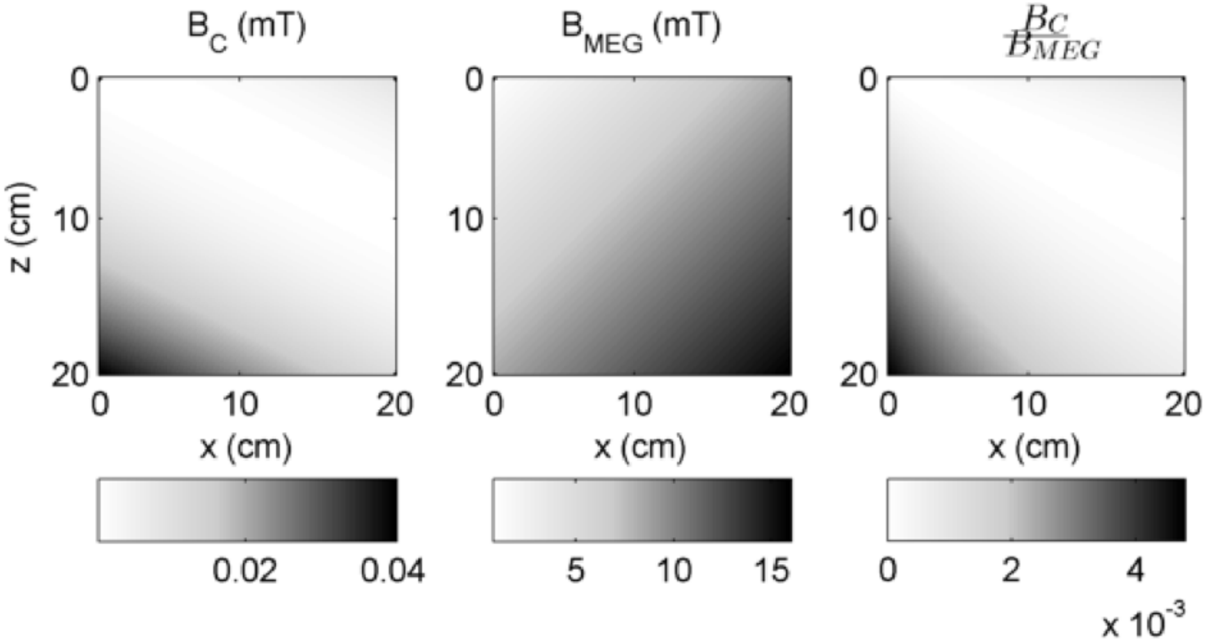

Figure 20: Figure on the left shows the B_C map, middle figure shows the B_{MEG} and figure on the right shows the ratio of B_C to B_{MEG}. $0 < x, z < 20cm$, $B_0 = 1.5$ Tesla, $G_x, G_z = 40$ milliTesla.

field with the strength of motion encoding gradient fields for a 1.5 Tesla human MRI system (Figure 20), these fields can be ignored for the current high field MRI systems.

7.3.4.2 Eddy Currents

Pulsed gradients induce eddy currents in the conducting structures of the magnet. This generates undesired time varying magnetic fields in the FOV. These unwanted magnetic fields decay multiexponentially with the time constants comparable to TE or even TR in some cases, which in return distorts the image.

Eddy currents can be compensated by adjusting the shape of the current function. Therefore, to generate a gradient pulse, a current shape consisting of three or more exponential functions are used (43). The amplitude and time constants of these exponential functions need to be tuned precisely to reduce the image artifacts due to eddy currents.

This is done with pre-emphasize circuitry. In human MRI scanners this process has been greatly improved since they need to run the gradients at high power and high switching rates all the time, as in EPI-based pulse sequences. But this may not be the case for animal scanners or smaller bore magnets.

Therefore, ULTIMATe MRE is expected to have less SNR than conventional MRE due to fact that it would cause more eddy currents. The strength of gradient power should be chosen carefully depending on the magnet, in order to get maximum encoding efficiency and maximum PNR.

7.4 Trade-Off between Time Efficiency and SNR Increase

Since MRI is one of the slowest imaging systems in clinical applications the time vs SNR trade-off is always an issue. Such trade-offs apply to MRE, where more time is needed.

It is already expected to have lower SNR with MRE due to longer TEs and MEGs. ULTIMATe MRE introduces more noise into system by means of eddy currents, diffusion and other reasons. On the other hand ULTIMATe MRE saves time by a factor of three in most cases. If we define the time efficiency as the number of motion information that can be encoded for given number of time steps, Table IV presents what would be the time efficiency of conventional MRE and ULTIMATe MRE for various times step values. So, instead of saving time, ULTIMATe

MRE can also be used to increase the SNR. If we use the SNR definition as signal strength S over σ, the standard deviation (Equation 7.3),

$$\mathbf{SNR} = \frac{S}{\sigma} = \frac{S}{\sqrt{\sigma^2}} \tag{7.3}$$

increasing the number of averages by utilizing the time saved can be written as follows

$$\mathbf{SNR} = \frac{nS}{\sqrt{n\sigma^2}} = \sqrt{n}\frac{S}{\sigma} \tag{7.4}$$

For $n = 3$ the ratio of the SNR of averaged ULTIMATe MRE and single conventional MRE will be as follows:

$$\mathbf{SNR}\text{ Ratio} = \frac{\sqrt{3}\ \mathbf{SNR}_{\text{ULTIMATe MRE}}}{\mathbf{SNR}_{\text{Conventional MRE}}} = \sqrt{3} \approx 1.73; \tag{7.5}$$

assuming ULTIMATe MRE and conventional MRE have the same variance. In practice this is not the case. It should be expected to have less SNR increase than $\sqrt{3}$ for three averages.

TABLE IV: Time Efficiency of MRE methods

Number of Time Steps	MRE	ULTIMATe-MRE
4	$\frac{1}{4} = 0.2500$	$\frac{1}{4} = 0.2500$
8	$\frac{1}{8} = 0.1250$	$\frac{3}{8} = 0.3750$
16	$\frac{1}{16} = 0.0625$	$\frac{7}{16} = 0.4375$
20	$\frac{1}{20} = 0.0500$	$\frac{9}{20} = 0.4500$
∞	$\frac{1}{\infty} = 0.0000$	$\frac{\infty}{2\infty} = 0.5000$

TABLE V: Minimum Increase in Echo Time (TE) Lookup Table for Three Directions

n	0	1	2	3	4	5	6	7
θ_1	0	$2\pi/8$	$4\pi/8$	$6\pi/8$	$8\pi/8$	$10\pi/8$	$12\pi/8$	$14\pi/8$
θ_1	0	$1\pi/4$	$1\pi/2$	$3\pi/4$	$1\pi/1$	$5\pi/4$	$3\pi/2$	$7\pi/4$
θ_1	0	$1\pi/4$	$1\pi/2$	$3\pi/4$	0	$1\pi/4$	$1\pi/2$	$3\pi/4$
θ_2	0	$4\pi/8$	$8\pi/8$	$12\pi/8$	$16\pi/8$	$20\pi/8$	$24\pi/8$	$28\pi/8$
θ_2	0	$1\pi/2$	$1\pi/1$	$3\pi/2$	0	$1\pi/2$	$1\pi/1$	$3\pi/2$
θ_2	0	$1\pi/2$	0	$1\pi/2$	0	$1\pi/2$	0	$1\pi/2$
θ_3	0	$6\pi/8$	$12\pi/8$	$18\pi/8$	$24\pi/8$	$30\pi/8$	$36\pi/8$	$42\pi/8$
θ_3	0	$3\pi/4$	$3\pi/2$	$1\pi/4$	$1\pi/1$	$3\pi/4$	0	$3\pi/4$
θ_3	0	$3\pi/4$	$1\pi/2$	$1\pi/4$	0	$3\pi/4$	0	$3\pi/4$
$\min\theta_1,\theta_2,\theta_3$	0	$1\pi/4$	0	$1\pi/4$	0	$1\pi/4$	0	$1\pi/2$
$\theta_1 - \min$	0	0	$1\pi/2$	$1\pi/2$	0	0	$1\pi/2$	$1\pi/4$
$\theta_2 - \min$	0	$1\pi/4$	0	$1\pi/4$	0	$1\pi/4$	0	0
$\theta_3 - \min$	0	$1\pi/2$	$1\pi/2$	0	0	$1\pi/2$	0	$1\pi/4$

CHAPTER 8

CONCLUSION

Simultaneous multi-directional MRE encoding has been considered to be unfeasible since the introduction of MRE, about 20 years ago. To solve this problem, we have developed two new methods to override this limitation and successfully encoded motion in three directions concurrently. The first method was multi-directional motion encoding (27) with a different frequency in each direction. The second method was introduced, shortly after the first method, and it enabled encoding a single frequency (29) for all three directions simultaneously. The first method is called Selective Spectral Displacement Projection, SDP-MRE. The latter one is called Sample Interval Modulation, SLIM-MRE.

In this study, the technique developed in SLIM-MRE was integrated into SDP-MRE to achieve the most general and optimal motion encoding MRE pulse sequence, Unified sampLing Time Interval ModulATion, ULTIMATe MRE. It is shown that, motion of any number of frequencies in any number of directions can be encoded simultaneously without any redundant time step, keeping the motion encoding efficiency as high as possible.

A comparison of ULTIMATe-MRE and conventional MRE was done on a homogeneous gel sample using a high field vertical MRI system. Performance was compared by calculating a shear modulus value via curve fitting the linear profiles taken from the wave image to the closed form solution of cylindrical wave propagation. Shear modulus estimations across the different method vary within the variance of each estimation.

ULTIMATe MRE has been demonstrated to reduce the scan time of MRE by reducing the necessary number of MRE scans by a factor of three compared to a conventional MRE protocol of 8 time steps without compromising the PNR on the wave images or performance on stiffness estimation.

APPENDICES

Appendix A

A GUIDE TO SNR

A.1 Introduction

Signal to noise ratio (SNR) is the ratio of the average power of the signal to the average power of the noise acquired at same time instances. If the mean values of both the signal and the noise are zero, SNR can be defined as ratio of the signal variance to the noise variance. In different applications the definition of the SNR may change depending on how the user defines the signal and the noise. In the following section, various SNR definitions are introduced for the different stages of the MRE process. These definitions are not absolute; they are presented to provide a guideline to users and present what an SNR value may mean depending on the stage of an MRE process.

A.2 SNR in MRE

In MRE, the term SNR can appear in several different stages of data acquisition and data processing, and each of them requires a different definition. These stages can be categorized into six groups. The first stage is creating FID, the second stage is digitizing FID, the third stage is constructing complex MRI image, the fourth stage is constructing wave images, the fifth stage is construction analytical wave image, and the final stage is stiffness map estimation. Although factors affecting SNR in the first, the second and the third stages are out of the scope of this dissertation, they are listed in order to understand the differences of the SNR in between stages. It should be noted that there are many more factors affecting the SNR, which are not necessary for the purpose of this chapter; hence, they are not introduced, but rather the main contributions are listed. Also, this compartmentalization of the whole MRE process is not unique; it is chosen this way to minimize ambiguity of the SNR term used in these stages.

In the first stage, the noise added to the FID ideally comes from thermal noise. However, in reality there are other factors contributing to noise originating from the artifacts in the magnetic fields (B0, B1, gradient fields), transmitter/receiver imperfections, filter non-linearity, errors originating from demodulation, etc. The SNR can be defined as the ratio of the average power of the FID to the average power of the noise sources mentioned above.

In the second stage, the FID is sampled and quantized. Besides the thermal noise added to the FID signal in analog circuitry components, sampling and quantization processes also introduce their own errors such as aliasing, aperture, jitter and quantization error. The definition of the SNR can be same as in the first stage but it is in discrete domain rather than continuous time domain.

In the third stage, the digitized FID is rearranged into k-space and then transformed to image space. Some transformation algorithms, which are not one-to-one, may introduce additional errors in the MRI image. Although power of the image data over the power of noise seems to be the definition of the SNR at this stage, the actual definition of SNR differs depending on what the user is looking for in the image. The reason for that is strong signals may saturate the analog to digital converter and can obscure the area user needs to analyze due to dynamic range of digitizer. Therefore, sometimes, it may be necessary to sacrifice the FID strength to unbury the hidden information in the FID signal. This can be done via adjusting some of the imaging parameters, such as but not limited to TR and TE. In another case, the user might be interested only in the phase part of complex MR image rather than the magnitude part of it. Therefore, SNR should be defined as the power of the information user looking for in the phase image over the power of noise in the phase image. A relation for the SNR and the PNR in MRI can be found in (44).

In the fourth stage the SNR definition is the ratio of the power of wave information in the wave image to the power of noise in the wave image. The wave images are created from the phase component of the complex MR images by linearly subtracting the phase part of two separate scans where every parameter of the scans are the same, other than polarization of the MEGs. Therefore, the SNR of the phase part of the complex MRI images directly affects the SNR of corresponding wave image. However, any coherent noise components that may exist in the phase components of the complex MR images, with different origin than MEGs, are eliminated by this linear subtraction operation. Hence, it is expected to have a higher value for SNR in a wave image than a simple averaging operation of two phase images.

The fifth stage, constructing the complex wave image, yields an improved SNR of the same kind as in stage four because complex wave images are obtained by combining coherent parts of wave images using either filtering or Fourier transform followed by frequency bin selection, which results in elimination of unwanted frequency components and the noise in that part of the spectrum.

Appendix A (Continued)

In the last stage, SNR cannot be measured in terms of the power of the stiffness map because values in the stiffness map indicate properties of material under investigation rather than any sort of signal strength. In other words, a lower value in a stiffness map doesn't mean weak signal but low stiffness in the respective voxel. On the other hand, it is viable to evaluate noise originating from stiffness map estimation algorithms due to imperfections in the algorithms themselves and/or the noise in the complex wave image, which is used as the input for stiffness map estimation algorithms. Hence, one can use the term SNR as inverse power of noise in this stage. Note that, in this stage SNR only depends on the noise generated by the inversion algorithm; so, we assume the signal has unity power.

In conclusion, in each stage of MRE, SNR may have different definitions because the definition of the signal and the noise changes throughout the stages. Therefore, when comparing multiple SNR values in a context, one must make sure that all the SNR values belong to the same stage of the MRE process.

Appendix B

PROGRAMMING MOTION ENCODING GRADIENTS

An example of how to create the Motion Encoding Gradients (MEGs) was given in the code below. The code was written in C programming language syntax, however, it can be easily translated into any other programming languages. Comments embedded into the code and explanatory variable names are sufficient for reader to examine and replicate the code.

```
/*----- Set MRE Parameters into D,L arrays ----*/
  ACQ_trim[10][0]=100;
  ACQ_trim[10][1]=100;
  ACQ_trim[10][2]=100;
  ACQ_trim[11][0]=100;
  ACQ_trim[11][1]=100;
  ACQ_trim[11][2]=100;
  ACQ_trim[12][0]=100;
  ACQ_trim[12][1]=100;
  ACQ_trim[12][2]=100;


  L[8]=1; /* Counter for 180 phase shift condition */
```

Appendix B (Continued)

```
/******* MRE Gradient Shape Functions***************************/

  int i, j, k, TotalGradientPoints;

  double SampleInterval;

  double t, pi, Tshift, f, T, delta, Ts_min;


  i=0; j=0; pi = 3.14;

  // *** Note that "MEGTotalDuration" is in miliseconds

  // Minimum time interval between points of a gradient shape,

  // limited by system

  Ts_min = 4e-3;

  // maximum points we can use to create gradient shape

  // for a give duration

  TotalGradientPoints=(int)floor(MEGTotalDuration/Ts_min);

  // this is the time between sample points

  // for calculated total gradient shape points

  SampleInterval = MREDuration/1000/TotalGradientPoints;


  // Create an Empty array for a single frequency temporary MEG

  double MonoMEG[TotalGradientPoints];


  // Following two lines are specific to Bruker system

  // (Can be safely ignored to understand the code)
```

Appendix B (Continued)

```
// total number of elements in gradient shape
L[12]=TotalGradientPoints;
// Number of time steps
L[7]=MEGTimeOffsetNum;

// These are 2D arrays which would have gradient shapes
// for each time steps
PARX_change_dims("MEGread" ,MEGTimeOffsetNum,TotalGradientPoints);
PARX_change_dims("MEGphase",MEGTimeOffsetNum,TotalGradientPoints);
PARX_change_dims("MEGslice",MEGTimeOffsetNum,TotalGradientPoints);

// Reset MEGread, MEGphase and MEGslice to zero
for (i=0;i<MEGTimeOffsetNum;i++)
{
  for (k=0;k<TotalGradientPoints;k++)
  {
    MEGread[i][k]=0;
    MEGphase[i][k]=0;
    MEGslice[i][k]=0;
  }
}

// Fill out mono MEG then place
```

Appendix B (Continued)

```
// it in MEGread, MEGphase and MEGslice
for (i=0;i<MEGTimeOffsetNum;i++)
{
  for (j=0;j<MEGFreqNum;j++)
  {
    f = MEGFreqList[j]; // Frequency
    T = (float)1/f; // Period
    // Requires time offset for given frequency and frequency bin
    Tshift=(float)MEGFreqBinPlacementList[j]*i/MEGTimeOffsetNum/f;

    for (k=0;k<TotalGradientPoints;k++)
    {
      // real time instance
      t = (float)k*SampleInterval;
      // shift amount in real time
      delta = t-(Tshift-T*(int)(Tshift/T));
      // Outside the given time MEG is zero
      if ((delta>=0)&&(f*delta<MEGNumList[j]))
              {
        MonoMEG[k]=(float)sin(2*pi*f*delta);
        //MEGPowerList is previously calculated, such that the
        //total power per gradient cannot be greater than 100
        MonoMEG[k]*=(float)MEGPowerList[j]/100; // Scale the power
```

```
        }
        else
        {
          MonoMEG[k]=0;
        };
        // Fill out MEGread, MEGphase and MEGslice
        switch ( MEGDirectionList[j] ){
                case DirectionRead:
                  MEGread[i][k]  += MonoMEG[k];
                  break;
                case DirectionPhase:
                  MEGphase[i][k] += MonoMEG[k];
                  break;
                case DirectionSlice:
                  MEGslice[i][k] += MonoMEG[k];
                  break;
                default:
                  DB_MSG(("**Error: Invalid direction "));
                  break;
        };};};};}
```

CITED LITERATURE

1. Muthupillai, R., Lomas, D., Rossman, P., Greenleaf, J., Manduca, A., and Ehman, R.: Magnetic resonance elastography by direct visualization of propagating acoustic strain waves. Science, 269(5232):1854–1857, 1995.

2. Glaser, K. J., Manduca, A., and Ehman, R. L.: Review of mr elastography applications and recent developments. Journal of Magnetic Resonance Imaging, 36(4):757–774, 2012.

3. Kut, C., Schneider, C., Carter-Monroe, N., Su, L.-M., Boctor, E., and Taylor, R.: Accuracy of localization of prostate lesions using manual palpation and ultrasound elastography. In SPIE Medical Imaging, pages 726128–726128. International Society for Optics and Photonics, 2009.

4. Harrild, D. M., Han, Y., Geva, T., Zhou, J., Marcus, E., and Powell, A. J.: Comparison of cardiac mri tissue tracking and myocardial tagging for assessment of regional ventricular strain. The International Journal of Cardiovascular Imaging, 28(8):2009–2018, 2012.

5. Nissi, M., Rieppo, J., Töyräs, J., Laasanen, M., Kiviranta, I., Nieminen, M., and Jurvelin, J.: Estimation of mechanical properties of articular cartilage with mri–dgemric,¡ i¿ t¡/i¿¡ sub¿ 2¡/sub¿ and¡ i¿ t¡/i¿¡ sub¿ 1¡/sub¿ imaging in different species with variable stages of maturation. Osteoarthritis and Cartilage, 15(10):1141–1148, 2007.

6. Yin, Z., Schmid, T., Yasar, T. K., Liu, Y., Royston, T. J., and Magin, R.: Mechanical characterization of tissue-engineered cartilage using microscopic magnetic resonance elastography (μmre). Tissue Engineering, (ja), 2013.

7. Yasar, T. K., Royston, T. J., and Magin, R. L.: A comparison of mechanical wave measurement techniques to quantify soft tissue viscoelasticity up to 8 khz: A phantom study of shear, rayleigh and lamb waves. The Journal of the Acoustical Society of America, 132(3):1981–1981, 2012.

8. Yasar, T. K., Royston, T. J., and Magin, R. L.: Wideband mr elastography for viscoelasticity model identification. Magnetic Resonance in Medicine, 70(2):479–489, 2013.

9. Yasar, T. K., Royston, T. J., and Magin, R. L.: Taking mr elastography (mre) to the microscopic scale (μmre). In Biomedical Imaging: From Nano to Macro, 2011 IEEE International Symposium on, pages 1618–1623. IEEE, 2011.

10. Wang, H., Weaver, J. B., Doyley, M. M., Kennedy, F. E., and Paulsen, K. D.: Optimized motion estimation for mre data with reduced motion encodes. Physics in Medicine and Biology, 53(8):2181, 2008.

11. Rump, J., Klatt, D., Braun, J., Warmuth, C., and Sack, I.: Fractional encoding of harmonic motions in mr elastography. Magnetic Resonance in Medicine, 57(2):388–395, 2007.

12. Klatt, D., Asbach, P., Rump, J., Papazoglou, S., Somasundaram, R., Modrow, J., Braun, J., and Sack, I.: In vivo determination of hepatic stiffness using steady-state free precession magnetic resonance elastography. Investigative Radiology, 41(12):841–848, 2006.

13. Yin, M., Talwalkar, J. A., Glaser, K. J., Manduca, A., Grimm, R. C., Rossman, P. J., Fidler, J. L., and Ehman, R. L.: Assessment of hepatic fibrosis with magnetic resonance elastography. Clinical Gastroenterology and Hepatology, 5(10):1207–1213, 2007.

14. Sinkus, R., Tanter, M., Xydeas, T., Catheline, S., Bercoff, J., and Fink, M.: Viscoelastic shear properties of in vivo breast lesions measured by mr elastography. Magnetic Resonance Imaging, 23(2):159–165, 2005.

15. Hirsch, S., Guo, J., Reiter, R., Papazoglou, S., Kroencke, T., Braun, J., and Sack, I.: Mr elastography of the liver and the spleen using a piezoelectric driver, single-shot wave-field acquisition, and multifrequency dual parameter reconstruction. Magnetic Resonance in Medicine, 71(1):267–277, 2014.

16. Murphy, M. C., Huston, J., Jack, C. R., Glaser, K. J., Manduca, A., Felmlee, J. P., and Ehman, R. L.: Decreased brain stiffness in alzheimer's disease determined by magnetic resonance elastography. Journal of Magnetic Resonance Imaging, 34(3):494–498, 2011.

17. Hirsch, S., Klatt, D., Freimann, F., Scheel, M., Braun, J., and Sack, I.: In vivo measurement of volumetric strain in the human brain induced by arterial pulsation and harmonic waves. Magnetic Resonance in Medicine, 70(3):671–683, 2013.

18. Johnson, C. L., McGarry, M. D., Gharibans, A. A., Weaver, J. B., Paulsen, K. D., Wang, H., Olivero, W. C., Sutton, B. P., and Georgiadis, J. G.: Local mechanical properties of white matter structures in the human brain. NeuroImage, 79:145–152, 2013.

19. Elgeti, T., Rump, J., Hamhaber, U., Papazoglou, S., Hamm, B., Braun, J., and Sack, I.: Cardiac magnetic resonance elastography: initial results. Investigative Radiology, 43(11):762–772, 2008.

20. Klatt, D., Hamhaber, U., Asbach, P., Braun, J., and Sack, I.: Noninvasive assessment of the rheological behavior of human organs using multifrequency mr elastography: a study of brain and liver viscoelasticity. Physics in Medicine and Biology, 52(24):7281, 2007.

21. Papazoglou, S., Hirsch, S., Braun, J., and Sack, I.: Multifrequency inversion in magnetic resonance elastography. Physics in Medicine and Biology, 57(8):2329, 2012.

22. Sack, I., Beierbach, B., Wuerfel, J., Klatt, D., Hamhaber, U., Papazoglou, S., Martus, P., and Braun, J.: The impact of aging and gender on brain viscoelasticity. Neuroimage, 46(3):652–657, 2009.

23. Wuerfel, J., Paul, F., Beierbach, B., Hamhaber, U., Klatt, D., Papazoglou, S., Zipp, F., Martus, P., Braun, J., and Sack, I.: Mr-elastography reveals degradation of tissue integrity in multiple sclerosis. Neuroimage, 49(3):2520–2525, 2010.

24. Freimann, F. B., Streitberger, K.-J., Klatt, D., Lin, K., McLaughlin, J., Braun, J., Sprung, C., and Sack, I.: Alteration of brain viscoelasticity after shunt treatment in normal pressure hydrocephalus. Neuroradiology, 54(3):189–196, 2012.

25. Perriñez, P. R., Pattison, A. J., Kennedy, F. E., Weaver, J. B., and Paulsen, K. D.: Contrast detection in fluid-saturated media with magnetic resonance poroelastography. Medical Physics, 37(7):3518–3526, 2010.

26. Othman, S. F., Xu, H., Royston, T. J., and Magin, R. L.: Microscopic magnetic resonance elastography (μmre). Magnetic Resonance in Medicine, 54(3):605–615, 2005.

27. Yasar, T. K., Klatt, D., Magin, R. L., and Royston, T. J.: Selective spectral displacement projection for multifrequency mre. Physics in Medicine and Biology, 58(16):5771, 2013.

28. Sack, I., Gedat, E., Bernarding, J., Buntkowsky, G., and Braun, J.: Magnetic resonance elastography and diffusion-weighted imaging of the sol/gel phase transition in agarose. Journal of Magnetic Resonance, 166(2):252–261, 2004.

29. Klatt, D., Yasar, T. K., Royston, T. J., and Magin, R. L.: Sample interval modulation for the simultaneous acquisition of displacement vector data in magnetic resonance elastography: theory and application. Physics in Medicine and Biology, 58(24):8663, 2013.

30. Graff, K. F.: Wave motion in elastic solids. Courier Dover Publications, 1975.

31. Suki, B., Barabasi, A.-L., and Lutchen, K. R.: Lung tissue viscoelasticity: a mathematical framework and its molecular basis. Journal of Applied Physiology, 76(6):2749–2759, 1994.

32. Craiem, D. and Armentano, R. L.: A fractional derivative model to describe arterial viscoelasticity. Biorheology, 44(4):251–263, 2007.

33. Rouse Jr, P. E.: A theory of the linear viscoelastic properties of dilute solutions of coiling polymers. The Journal of Chemical Physics, 21(7):1272–1280, 1953.

34. Shaw, M. T. and MacKnight, W. J.: Introduction to polymer viscoelasticity. John Wiley & Sons, 2005.

35. Royston, T. J., Dai, Z., Chaunsali, R., Liu, Y., Peng, Y., and Magin, R. L.: Estimating material viscoelastic properties based on surface wave measurements: A comparison of techniques and modeling assumptions. The Journal of the Acoustical Society of America, 130(6):4126–4138, 2011.

36. Magin, R. L.: Fractional calculus in bioengineering. Begell House Redding, 2006.

37. Kiss, M. Z., Varghese, T., and Hall, T. J.: Viscoelastic characterization of in vitro canine tissue. Physics in medicine and biology, 49(18):4207, 2004.

38. Oliphant, T. E., Manduca, A., Ehman, R. L., and Greenleaf, J. F.: Complex-valued stiffness reconstruction for magnetic resonance elastography by algebraic inversion of the differential equation. Magnetic Resonance in Medicine, 45(2):299–310, 2001.

39. Oppenheim, A. V., Schafer, R. W., and Buck, J. R.: Discrete-Time Signal Processing (2nd Edition), chapter 11, pages 775–802. Prentice Hall, 2 edition, January 1999.

40. Kolipaka, A., McGee, K. P., Araoz, P. A., Glaser, K. J., Manduca, A., Romano, A. J., and Ehman, R. L.: Mr elastography as a method for the assessment of myocardial stiffness: Comparison with an established pressure–volume model in a left ventricular model of the heart. Magnetic Resonance in Medicine, 62(1):135–140, 2009.

41. Sack, I., Mcgowan, C. K., Samani, A., Luginbuhl, C., Oakden, W., and Plewes, D. B.: Observation of nonlinear shear wave propagation using magnetic resonance elastography. Magnetic Resonance in Medicine, 52(4):842–850, 2004.

42. Bernstein, M. A., Zhou, X. J., Polzin, J. A., King, K. F., Ganin, A., Pelc, N. J., and Glover, G. H.: Concomitant gradient terms in phase contrast mr: analysis and correction. Magnetic Resonance in Medicine, 39(2):300–308, 1998.

43. Jehenson, P., Westphal, M., and Schuff, N.: Analytical method for the compensation of eddy-current effects induced by pulsed magnetic field gradients in nmr systems. Journal of Magnetic Resonance (1969), 90(2):264–278, 1990.

44. Bernstein, M., King, K., and Zhou, X.: Handbook of MRI pulse sequences.. Burlington: Elsevier Academic Press, 2004.